CHAPTER 18

Diffuse Optical Tomography of the Breast

Regine Choe and Arjun G. Yodh

Department of Physics and Astronomy, University of Pennsylvania, Philadelphia, PA 19104, USA

CONTENTS

1. INTRODUCTION

Approximately one in nine women will develop breast cancer in her lifetime, and of these cancers, approximately 30% will be fatal [1, 2]. Currently, several clinical methods are used in breast cancer screening and diagnosis [3, 4]. The most common, and arguably the most effective screening technique at this time is X-ray mammography. X-ray mammography, however, has a ~22% false negative rate in women under 50 [5], and sometimes it cannot accurately distinguish between benign and malignant tumors [6]. X-ray mammography has been shown in recent studies to have lower sensitivity in pre-menopausal women [4] and to be of limited clinical value for women under 35 years of age [7]. Furthermore, increased mammographic density can arise in some post-menopausal women, for example, due to hormone replacement therapy [8] or cyclically during the menstrual cycle of younger women [9]. These effects reduce the effectiveness of mammographic screening. Techniques such as ultrasound and magnetic resonance imaging (MRI) are sometimes used in addition to X-ray mammography, but they have limitations such as high cost, low throughput, limited specificity (MRI), and low sensitivity (ultrasound). Thus it remains desirable to detect cancers earlier for treatment [10, 11], to detect cancers missed by mammography [12–14], and to add specificity to the mix because the majority of invasive follow-up procedures (e.g., surgical biopsies) are performed on normal or benign tissue [15].

ISBN:1-58883-090-X

Emerging Technology in Breast Imaging and Mammography
Edited by Jasjit Suri, Rangaraj M. Rangayyan, and Swamy Laxminarayan
Pages:317–342

Near-infrared (NIR) diffuse optical tomography (DOT) and spectroscopy (DOS) are diagnostic tools that rely on functional processes for contrast. These techniques provide several unique measurable parameters with the potential to enhance breast tumor sensitivity and specificity. They utilize non-ionizing radiation, they are noninvasive, and they are often technologically simple and fast. DOT and DOS are attractive for applications that require frequent monitoring of physiological parameters, for example for monitoring cancer therapies. Finally, their utility is not limited to older women, which is the case with X-ray mammography.

Diffuse optical tomography and spectroscopy measure tissue optical absorption coefficients, which, in turn, provide access to blood dynamics, total hemoglobin concentration (*THC*), tissue blood oxygen saturation (StO_2), and water (H_2O) and lipid content. These tissue properties are often substantially different in rapidly growing tumors compared to normal tissues. For example, high concentrations of hemoglobin with low oxygen saturation are suggestive of rapidly growing tumors [16–19] due to their high metabolic demand and, sometimes, poor perfusion. Angiogenesis in tumors (quantifiable by *THC*) is an independent prognostic indicator [19], and the oxygenation status of tumors is known to have a close relationship with treatment efficacy [20]. In a different vein, an overall increase in organelle population due to proliferation of cancer cells may lead to an increase of optical scattering coefficients for the tumor. Nuclei and mitochondria are major contributors to optical scattering coefficients [21] as well as collagen in the extracellular matrix [22]. Finally, optical absorption, fluorescence, and scattering of exogenous contrast agents that occupy vascular and extravascular space also provide useful forms of sensitization.

Diffuse optical tomography and spectroscopy utilize photons in the near-infrared spectral window of 600–1000 nm, wherein photon transport in tissue is dominated by scattering rather than absorption. Photons experience multiple scattering events as they propagate deeply into tissue (up to ~10 cm). The primary chromophores in this spectral window are oxygenated hemoglobin (HbO_2), deoxygenated hemoglobin (Hb), water and lipid, each with a distinct spectrum. Accurate retrieval of tissue properties based on diffuse optical measurements requires that absorption and scattering be decoupled. A light transport model based on the diffusion approximation [23] is widely used to describe photon propagation through tissues in the NIR. Optical measurements at multiple source-detector positions on the tissue surfaces can be used with this model to reconstruct the internal distribution of the absorption coefficient (μ_a) and the reduced scattering coefficient (μ_s') in three-dimensions (3D). Physiological images of total hemoglobin concentration, blood oxygenation, water, and lipid are then derived from this information. Thus far, DOT and DOS have generated a great deal of scientific interest and have been applied in a variety of deep-tissue contexts including breast cancer imaging [24–40], brain functional spectroscopy and imaging [41–54], muscle functional studies [55–67], photodynamic therapy [68, 69], and radiation therapy monitoring [70].

The use of light to detect tumors in the breast was first proposed by Cutler in 1929 [71]. Cutler aimed to distinguish between solid tumors and cysts in the breast, but found it difficult to produce the necessary light intensity without exposing the patient's skin to extreme heat. In the early 1980's, however, essentially the same class of transillumination measurement was renewed [6, 72–81] using light in regions of low tissue absorption (i.e., 600 nm to 1300 nm). Unfortunately the high degree of breast tissue scattering distorted spectroscopic information and blurred optical images as a result of the large distribution of photon pathways through the tissue. The mathematical modeling of light transport in tissues had not been developed sufficiently for optical tomography to be readily employed.

As a result of numerous scientific and technological advances in tissue optics since 1990, optical mammography now appears feasible with levels of specificity and resolution superior to early work. The most critical advance in the field of photon migration has been the recognition and widespread acceptance that light transport over long distances in tissues is well approximated as a diffusive process [82–84]. Using this physical model, it is possible to quantitatively separate tissue scattering from tissue absorption and to accurately incorporate the influence of boundaries, such as the air-tissue interface, into the transport theory [85, 86]. Waves of diffuse light energy density [87] or their time-domain analogs [85, 88–90] propagate deeply in tissues (e.g. ~10 cm) and obey rules such as refraction [91], diffraction [92, 93], interference [94], and dispersion [95, 96] as they encounter variations in tissue properties. The separation of scattering and absorption afforded by the diffusion approximation has led to new, quantitative investigations about the average concentrations of molecular species in a variety of highly scattering media [85, 96–104].

During the last few years, scientists in the field have begun to experimentally revisit the problem of optical mammography armed with these new ideas and approaches. Experimenters have begun to exploit the full possibilities of the tomographic approach with emphasis on clinical measurements. The photon migration community, especially in breast cancer imaging, is now poised to identify and characterize tumor contrast. Photon migration breast cancer research is evolving toward better quantification (3D imaging with multiple source detector positions), extensive exploration of physiological parameters (via multiple wavelength spectroscopy, and correlation with histo-pathology [28, 105, 106]), co-registration with other imaging modalities, and therapy monitoring.

In this chapter, the theory and instrumentation of DOT will be briefly outlined. Then some clinical results connected with the breast cancer application will be discussed, including: (1) bulk optical/physiological properties of healthy breasts, (2) three-dimensional reconstructed breast cancer imaging based on endogenous contrast, (3) optical detection of blood flow in

reast cancer, (4) neoadjuvant chemotherapy monitoring, (5) naging based on exogenous contrast (a step toward molecular imaging), and (6) co-registration with other imaging nodalities.

The aim of this chapter is to provide a snapshot of the field. t is not intended as a comprehensive review of the field, and eaders are encouraged to read other review articles [45, 84, 07, 108] as well as the primary publications to gain a full erspective.

2. THEORY

2.1. Photon Propagation

The propagation of photons through turbid media such as tissue is often described by the Boltzman transport equation [109, 110], but solutions of the Boltzman equation are computationally intensive and time consuming. Fortunately, for most DOT applications, the Boltzman transport equation is well approximated by the photon diffusion equation. A clear derivation of the photon diffusion equation from the transport equation is given in reference [111]. Here we adopt the photon diffusion equation as our starting point. The photon diffusion equation has the following form:

$$\nabla \cdot (D(\mathbf{r})\nabla\Phi(\mathbf{r},t)) - \mu_a(\mathbf{r})\Phi(\mathbf{r},t) - \frac{1}{v}\frac{\partial\Phi(\mathbf{r},t)}{\partial t} = -S(\mathbf{r},t). \tag{1}$$

Here $\mathbf{r}$ is the position vector, t is time, and v is the speed of light in the medium [cm/s]. $D(\mathbf{r}) \cong \frac{1}{3\mu_s'(\mathbf{r})}$ [112] is the photon diffusion coefficient, $\mu_s'(\mathbf{r})$ [cm^{-1}] is the reduced scattering coefficient, and $\mu_a(\mathbf{r})$ [cm^{-1}] is the absorption coefficient. $\Phi(\mathbf{r},t)$ is the photon fluence rate [Watt/cm^2] and $S(\mathbf{r},t)$ is the isotropic light source term [Watt/cm^3].

The behavior of $\Phi(\mathbf{r},t)$ near the boundary of the turbid medium is described by partial current boundary conditions (i.e. mixed Dirichlet-Neuman boundary condition) [23, 113–115],

$$\frac{\partial\Phi(\mathbf{r})}{\partial\hat{n}} = -\alpha\Phi(\mathbf{r}), \tag{2}$$

where $\hat{n}$ is the vector normal to measurement boundary, α is related to the refractive index mismatch at boundary via the following: $\alpha = \left(\frac{1-R_{eff}}{1+R_{eff}}\right)\frac{3\mu_s'}{2}$, $R_{eff} \sim \frac{-1.44}{n^2} + \frac{0.71}{n} + 0.668 + 0.063n$ and $n = \frac{n_{in}}{n_{out}}$ [113, 116]. Typically, the source fiber on the surface is modeled as a single isotropic point source placed a distance $1/\mu_s'$ into the medium from the surface.

Three types of measurements are used: continuous-wave (CW), frequency-domain (FD), and time-domain (TD) measurements. Figure 1 schematically illustrates the input light source (solid line) and the output signal (dotted line) for each measurement type. Continuous-wave measurements employ a light source whose intensity does not vary with time; the detector measures the transmitted intensity, which is affected by the medium. Frequency-domain measurements employ a light source that is amplitude modulated in the radio-frequency (RF) range. The detector measures the amplitude of the transmitted diffuse photon density wave and its phase-shift relative to the input. Time-domain measurements employ a short input light pulse (i.e. typically less than 1 nanosecond) and detect a delayed and temporally broadened output pulse.

2.2. Forward/Inverse Problem

The goal of diffuse optical tomography (DOT) is to accurately estimate the distribution of optical properties in a tissue volume from noninvasive optical measurements on the surface of the medium. Various algorithms can be utilized to estimate optical properties [107]. These algorithms differ depending on the choice of photon propagation model, measurement type and geometry, and optimization scheme. A generalized outline of iterative model-based optical properties reconstruction is described in the flow chart in Figure 2.

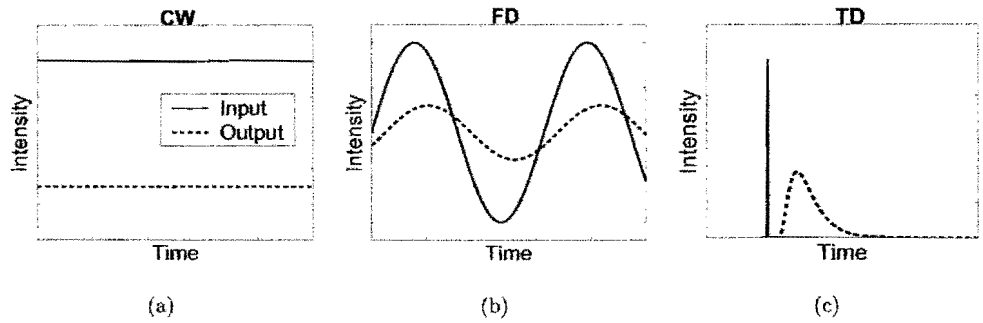

Figure 1. Measurement types: (a) Continuous-wave (CW), (b) Frequency-domain (FD), (c) Time-domain (TD) measurement types (solid line: input light source, dashed line: output detected signal). CW measurements employ a light source whose intensity does not vary with time. FD measurements employ a light source whose amplitude is modulated with radio-frequency and a detection system to measure intensity decrease and phase-shift of the output. TD measurements employ a short input light pulse and detect a delayed and temporally broadened output pulse.

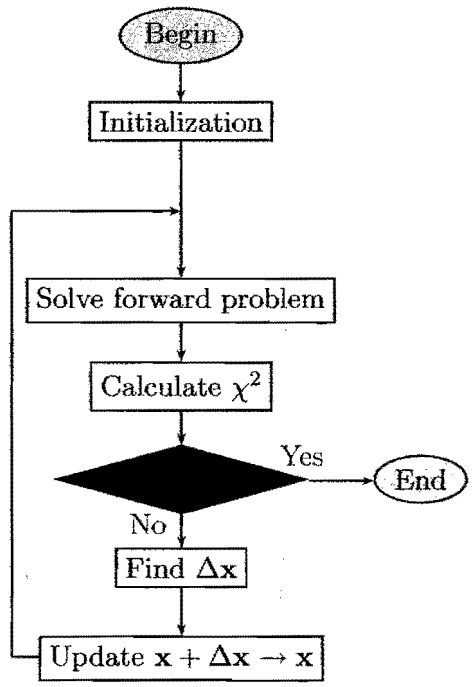

Figure 2. General analysis flow chart for iterative model-based optical properties reconstruction. $\mathbf{x}$ is a vector of unknown properties (e.g., μ_a and μ_s'). To solve the forward problem is to compute the fluence rate on the sample surface for given spatial distribution of $\mathbf{x}$. χ^2 is the objective function that quantifies the discrepancy between the calculated and measured fluence rate. At each iteration, $\Delta\mathbf{x}$, which will cause χ^2 to decrease compared to the previous value, is calculated.

Here $\mathbf{x}$ is a vector of unknown properties. For a measurement using a single optical wavelength, $\mathbf{x}$ is a vector of absorption (μ_a) and scattering (μ_s') factors in each voxel of the reconstruction volume. For measurements employing many optical wavelengths, $\mathbf{x}$ is more often a vector of chromophore concentration (C_l), scattering prefactor (A) and scattering power (b) in each volume element. See Equations 10 and 11 for precise definitions of A, b and C_l. The initialization process consists of reading in the measurement data, defining the reconstruction space, and assigning initial guess for $\mathbf{x}(\mathbf{r})$. $\mathbf{r}$ denotes position within the sample volume. The forward problem computes the fluence rate, $\Phi(\mathbf{r})$, on the sample surface given light source information and optical property distribution $\mathbf{x}(\mathbf{r})$. χ^2 quantifies the discrepancy between the calculated and measured fluence rate; its value determines whether to update $\mathbf{x}(\mathbf{r})$ and iterate again or to stop the calculation. If the stopping criteria is not met, the inverse problem estimates a change in optical properties, $\Delta\mathbf{x}$, based on χ^2 for the next iteration.

The inverse problem can be formulated in various ways. Diffuse optical *spectroscopy* treats the reconstruction space as either homogeneous or composed of a limited number of piecewise homogeneous regions. Therefore, the number of unknowns (i.e., the bulk optical properties of each region) is usually much less than the number of measurements. For diffuse optical *tomography*, the reconstruction volume is discretized into large number of volume elements or voxels, and the optical properties of each voxel are the unknowns to be reconstructed.

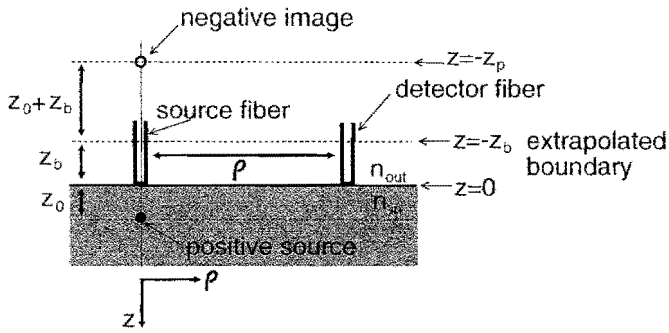

Figure 3. Source and image configuration for a semi-infinite homogeneous medium using the extrapolated boundary condition. For the extrapolated boundary condition, the fluence rate is set to zero at an extrapolated boundary located at $z = -z_b$.

2.3. Diffuse Optical Spectroscopy (DOS)

Analytic solutions of the forward problem exist for simple measurement geometries such as infinite, semi-infinite, slab, cylinder, multiple layers, and a slab with an inclusion [117–121]. In this section, an analytic solution for semi-infinite geometry with extrapolated boundary condition is described. This approach is widely used in most DOS analyses.

For the extrapolated boundary condition [23, 122–124], the fluence rate is set to zero at an extrapolated boundary located at a distance z_b outside the medium i.e., $\Phi(\rho, z = -z_b) = 0$. The method of images depicted in Figure 3 can be used to construct the solution by placing a negative image source at the opposite side of the extrapolated boundary. In this extrapolated boundary case, the position of negative image source is at $-z_p = -(z_0 + 2z_b)$.

The analytic frequency-domain solution for the semi-infinite geometry with extrapolated boundary conditions is [117, 118]

$$\Phi(\rho, z) = \frac{S_0}{4\pi D}\left(\frac{exp(ik\sqrt{\rho^2 + (z - z_0)^2})}{\sqrt{\rho^2 + (z - z_0)^2}} - \frac{exp(ik\sqrt{\rho^2 + (z + z_p)^2})}{\sqrt{\rho^2 + (z + z_p)^2}}\right) \quad (3$$

where S_0 is the light source strength in [Watt], $k^2 = \frac{-v\mu_a + i\omega}{vD}$, ω is the modulation frequency, $z_0 = \frac{1}{\mu_s'}$, $z_p = z_0 + 2z_b$, $z_b = \frac{2}{3\mu_s'}\frac{1+R_{eff}}{1-R_{eff}}$, and $R_{eff} = -1.44/n^2 + 0.71/n + 0.668 + 0.063n$. The z axis is perpendicular to the medium,

and ρ is the radial distance parallel to the medium, as can be seen in Figure 3. The filled circle represents the light source displaced $\frac{1}{\mu_s'}$ inside the medium [85], and the open circle is the imaginary negative source displaced an equal distance (z_b) away from the extrapolated boundary where the fluence rate becomes zero.

2.4. Diffuse Optical Tomography (DOT)

There are excellent reviews on optical tomography method by S. R. Arridge [107, 108]. In this section, the methods widely used for breast cancer imaging will be briefly summarized.

A schematic description of DOT is given in Figure 4. The aim is to reconstruct the internal distribution of optical properties within the turbid medium (e.g., breast) by injecting light on the surface and detecting light that has propagated through the medium to another point on the surface.

Numerical techniques such as the finite difference method (FDM) or finite element method (FEM) are utilized to compute the forward problem (i.e., calculate the fluence rate at the surface) for an experimental geometry with complex distribution of optical properties. That is, $\Phi(\mathbf{r})$ is calculated from a matrix equation constructed by discretizing Equation 1 in combination with the partial current boundary condition (Eq. 2) for given $\mu_a(\mathbf{r})$ and $\mu_s'(\mathbf{r})$ distributions.

The goal of diffuse optical tomography is to find the optical properties distribution that best suits the measurements by optimizing an objective function, χ^2. In formulating the inverse problem, two common approximations are used for $\Phi(\mathbf{r})$: the Born and the Rytov expansions [125, 126]. In the Born approximation, $\Phi(\mathbf{r}, \mathbf{r}_s)$ is written as a linear superposition of incident (background, Φ_0) and scattered (heterogeneous, Φ_{sc}) diffusive waves: $\Phi(\mathbf{r}, \mathbf{r}_s) = \Phi_0(\mathbf{r}, \mathbf{r}_s) + \Phi_{sc}(\mathbf{r}, \mathbf{r}_s)$, where $\mathbf{r}_s$, is the source position. In the Rytov approximation, the contributions from the incident and scattered parts are expressed in exponential fashion: $\Phi(\mathbf{r}, \mathbf{r}_s) = exp[\Phi_0(\mathbf{r}, \mathbf{r}_s) + \Phi_{sc}(\mathbf{r}, \mathbf{r}_s)]$. An equation that provides the update scheme for the optical properties is readily derived using the diffusion equation, Green's theorem, and the Born/Rytov expansion. For example, for frequency-domain measurements with the modulation frequency ω, the Rytov expansion-based equation has the following form [127–131],

$$\frac{\int \nabla G(\mathbf{r}_d, \mathbf{r}) \cdot \nabla \Phi_c(\mathbf{r}, \mathbf{r}_s) \Delta D(\mathbf{r}) d^3r + \int G(\mathbf{r}_d, \mathbf{r}) \Phi_c(\mathbf{r}, \mathbf{r}_s) \Delta \mu_a(\mathbf{r}) d^3r}{\Phi_c(\mathbf{r}_d, \mathbf{r}_s)} = -ln\left(\frac{\Phi_m(\mathbf{r}_d, \mathbf{r}_s)\Phi_c^R(\mathbf{r}_d, \mathbf{r}_s)}{\Phi_m^R(\mathbf{r}_d, \mathbf{r}_s)\Phi_c(\mathbf{r}_d, \mathbf{r}_s)}\right) \quad (4)$$

where the Green's function, G, is the solution to

$$\nabla \cdot (D(\mathbf{r})\nabla G(\mathbf{r})) - \left(\mu_a(\mathbf{r}) - \frac{i\omega}{v}\right) G(\mathbf{r}) = -\delta(\mathbf{r}_d, \mathbf{r}), \quad (5)$$

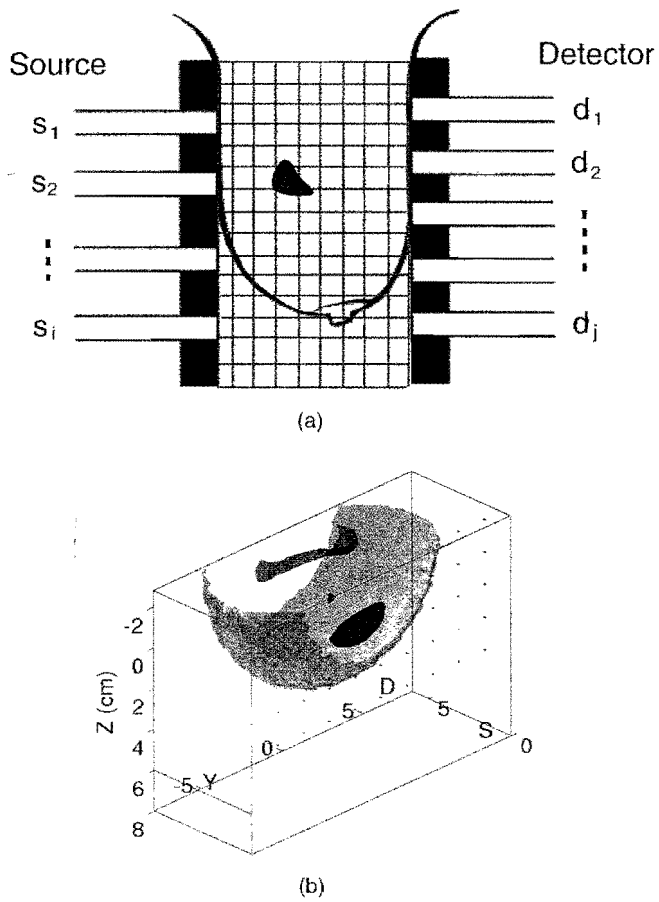

Figure 4. Schematic of diffuse optical tomography. (a) A breast with tumor is placed between source and detector plate as shown. Measurements from different source-detector pairs on the surface of the breast enable reconstruction of the spatial distribution of internal optical properties. (b) An example of lesion and breast boundary differentiation derived from 3D total hemoglobin concentration images. The light-colored isosurface shows the compressed breast and the darkest isosurface (near source plane S) shows an invasive ductal carcinoma. The medium-colored isosurface (near detector plane D) shows benign proliferative disease.

for the sample medium. Here $\Delta\mu_a(\mathbf{r}) = \mu_a(\mathbf{r}) - \mu_a^0(\mathbf{r})$ and $\Delta D(\mathbf{r}) = D(\mathbf{r}) - D^0(\mathbf{r})$ where the background absorption and scattering optical property distribution are $\mu_a^0(\mathbf{r})$ and $D^0(\mathbf{r})$. $\mathbf{r}_d$ is the detector position. Φ_m is the measured fluence rate and Φ_c is the calculated fluence rate based on the forward problem. Φ_m^R and Φ_c^R are the measured and calculated fluence rates for reference measurements.

Inversion methods used in breast cancer imaging are generally linear and nonlinear. The linear method is a single-step inversion of the linearized equation $\mathbf{J}\Delta\mathbf{x} = \mathbf{y}$ where $\Delta\mathbf{x}$ represents the change in the optical properties from an initial estimate (e.g., $\Delta\mu_a$ and $\Delta\mu_s'$). $\mathbf{J}$ is the Jacobian matrix relating the data and the unknowns, and $\mathbf{y}$ is difference between the

measured data and the calculated estimate [126]. For example, for Rytov approximation, the following linear equation can be derived from Equation 4

$$\begin{pmatrix} \frac{G\Phi|_{r_1}}{\Phi} & \cdots & \frac{G\Phi|_{r_N}}{\Phi} & \frac{\nabla G\cdot\nabla\Phi|_{r_1}}{\Phi} & \cdots & \frac{\nabla G\cdot\nabla\Phi|_{r_N}}{\Phi} \\ \vdots & & \vdots & \vdots & & \vdots \end{pmatrix} \times \begin{pmatrix} \Delta\mu_a(r_1) \\ \vdots \\ \Delta\mu_a(r_N) \\ \Delta D(r_1) \\ \vdots \\ \Delta D(r_N) \end{pmatrix} = \begin{pmatrix} -ln\left(\frac{\Phi_m}{\Phi_m^R}\frac{\Phi_c^R}{\Phi_c}\right)_{s=1,d=1} \\ -ln\left(\frac{\Phi_m}{\Phi_m^R}\frac{\Phi_c^R}{\Phi_c}\right)_{s=1,d=2} \\ -ln\left(\frac{\Phi_m}{\Phi_m^R}\frac{\Phi_c^R}{\Phi_c}\right)_{s=N_s,d=N_d} \end{pmatrix} \quad (6)$$

where s and d denotes source and detector indices, N_s, N_d are total number of source and detectors respectively, N is the total number of voxels, and r_1 to r_N represent positions of the voxel in the sample.

The nonlinear method is generally an iterative optimization of χ^2. Here we briefly outline two different approaches. One approach is to invert **J** iteratively (e.g., the Newton method [132]) and check the stopping criteria with respect to χ^2 at each iteration. Another approach uses the gradient of χ^2 to generate a minimum search direction without building **J** [133]. χ^2 defined in the Rytov fashion has the form

$$\chi^2 = \frac{1}{2}\sum_{s=1}^{N_s}\sum_{d=1}^{N_d}\left[ln\left(\frac{\Phi_m(\mathbf{r}_d,\mathbf{r}_s)\Phi_c^R(\mathbf{r}_d,\mathbf{r}_s)}{\Phi_m^R(\mathbf{r}_d,\mathbf{r}_s)\Phi_c(\mathbf{r}_d,\mathbf{r}_s)}\right)\right]^2 \quad (7)$$

Then the gradients of χ^2 become

$$\left.\frac{\partial\chi^2}{\partial\mu_a}\right|_{\mathbf{r}} = \sum_{s=1}^{N_s}\sum_{d=1}^{N_d} ln\left(\frac{\Phi_m(\mathbf{r}_d,\mathbf{r}_s)\Phi_c^R(\mathbf{r}_d,\mathbf{r}_s)}{\Phi_m^R(\mathbf{r}_d,\mathbf{r}_s)\Phi_c(\mathbf{r}_d,\mathbf{r}_s)}\right)\frac{1}{\Phi_c(\mathbf{r}_d,\mathbf{r}_s)} \times G(\mathbf{r}_d,\mathbf{r})\Phi_c(\mathbf{r},\mathbf{r}_s), \quad (8)$$

$$\left.\frac{\partial\chi^2}{\partial D}\right|_{\mathbf{r}} = \sum_{s=1}^{N_s}\sum_{d=1}^{N_d} ln\left(\frac{\Phi_m(\mathbf{r}_d,\mathbf{r}_s)\Phi_c^R(\mathbf{r}_d,\mathbf{r}_s)}{\Phi_m^R(\mathbf{r}_d,\mathbf{r}_s)\Phi_c(\mathbf{r}_d,\mathbf{r}_s)}\right)\frac{1}{\Phi_c(\mathbf{r}_d,\mathbf{r}_s)} \times \nabla G(\mathbf{r}_d,\mathbf{r})\cdot\nabla\Phi_c(\mathbf{r},\mathbf{r}_s). \quad (9)$$

The key reason to employ this gradient method is that the adjoint solution G is replaced by the solution for the weighted sum of all detectors, which can be computed directly by the forward solver without building **J**. Once the gradient vector is computed, any gradient-based generic algorithm can be applied to find the minimum of χ^2.

In terms of quantification, nonlinear methods are preferred because the inverse problem is intrinsically nonlinear. However, the nonlinear schemes are computationally intensive. Reconstruction algorithms used by major groups working on clinical breast cancer imaging are summarized in Table I.

Table 1. Comparison of clinical instruments for breast cancer application developed in the photon migration field. N_s: number of sources, N_d: number of detectors, N_λ: number of wavelength, T: acquisition time. Tandem configuration refers to the scanning of a pair of a source and a detector placed directly across at the shortest distance of the slab. Off-axis tandem configuration has a source and multiple detectors as a scanning pair. (CW: continuous-wave, FD: Frequency-domain, TD: Time-domain method, DPF: Differential pathlength factor, PCA: Principal components analysis, DOS: Diffuse optical spectroscopy)

Group	Type	Ns	N_d	N_λ	T	Geometry	Algorithm
Chance et al. [40]	CW	1	8	3	10 s	remission	DPF
Lilge et al. [134]	CW	1	1	145	2 min	remission	PCA
ViOptix, Inc. [135]	CW	8	8	2	NA	remission	DOS
Barbour et al. [136]	CW	25	32	4	0.32 s	cone	Linear
Phillips, Corp. [25]	CW	225	225	3	6 min	cone	Linear
Jiang et al. [137]	CW	64	64	3	12 min	rings	Nonlinear
Pogue et al. [138]	FD	16	45	6	30 s	rings	Nonlinear
Zhu et al.[139]	FD	12	8	2	NA	remission	Nonlinear
Carl Zeiss [24]	FD	1	2340	2	3 min	parallel, tandem	gating
Siemens [140]	FD	1	~7000	4	2 min	parallel, tandem	gating
Boas et al. [141]	FD	40	9	2	1.5 min	parallel-plate	Linear
Chance/Yodh et al. [26]	TD	24	8	1	80 s	parallel-plate	Linear
Cubeddu et al. [142]	TD	1	3000	4	5 min	parallel, tandem	gating/analytic
Rinneberg et al. [143]	TD	1	2000	2	5 min	parallel, tandem	gating/analytic
Rinneberg et al. [144]	TD	1	~6000	4	5–7 min	parallel, off-axis tandem	Linear
Hebden et al. [145]	TD	32	32	1	~10 min	rings	Nonlinear
ART, Inc. [36]	TD	1	1520	4	~8 min	parallel, off-axis tandem	Linear
Tromberg et. al. [146]	CW	1	1	2048	10 s	remission	DOS
	FD	1	1	7	30 s	line-scan	
Yodh et al. [147]	CW	48	2.28×10^5	6	8.4 min	parallel-plate	Nonlinear
	FD	48	9	4	—		

2.5. Physiological Parameters

After reconstruction of optical properties (μ_a, μ_s') at each wavelength, chromophore concentrations can be extracted from the total absorption using

$$\mu_a(\lambda, \mathbf{r}) = \sum_{l=1}^{L} \epsilon_l(\lambda) C_l(\mathbf{r}). \tag{10}$$

Here $\epsilon_l(\lambda)$ is the extinction coefficient, $C_l(\mathbf{r})$ is the concentration of the l^{th} chromophore, and L is the total number of chromophores. In the physiological case, major chromophores are oxygenated hemoglobin, deoxygenated hemoglobin, water and lipid. The extinction coefficients, $\epsilon_{Hb}, \epsilon_{HbO_2}, \epsilon_{H_2O}, \epsilon_{lipid}$ only depend on wavelength λ and have dimensions of $[\text{cm}^{-1}\mu\text{M}^{-1}]$. The extinction coefficients are well documented in the literature [148] (http://omlc.ogi.edu/spectra/). The concentrations of these chromophores C_{Hb}, C_{HbO_2}, C_{H_2O}, C_{lipid} are usually given in $[\mu\text{M}]$.

Scattering in tissue follows a simplified Mie-scattering approximation [149, 150] reasonably well, i.e.,

$$\mu_s'(\lambda, \mathbf{r}) = A(\mathbf{r})\lambda^{-b(\mathbf{r})}, \tag{11}$$

where $A(\mathbf{r})$ is called the scattering prefactor and $b(\mathbf{r})$ is called the scattering power (and is related to the particle size and density, index of refraction of scatterers, and the medium).

In conventional schemes as described above (which we will denote as the single-spectral method), absorption $(\mu_a(\mathbf{r}))$ and scattering coefficients $(\mu_s'(\mathbf{r}))$ at each wavelength are first determined from the reconstruction, and then the resulting absorption coefficients are used to extract chromophore concentrations using Equation 10. In the multi-spectral method (or the *a priori spectral* approach), the chromophore concentrations and scattering properties are reconstructed directly in a single step using data at all wavelengths with spectral constraints (Eqs. 10 and 11). The multi-spectral method [151–156] has gained attention recently because it reduces inter-parameter crosstalk [151, 155] and enables unique solutions, even for CW imaging [152, 154].

Once chromophore concentrations are obtained, more familiar physiological parameters may be derived, e.g., the total hemoglobin concentration $THC = C_{Hb} + C_{Hbo_2}$ and the tissue blood oxygen saturation $StO_2 = C_{HbO_2}/THC$.

2.6. Diffuse Correlation Spectroscopy (DCS)

Until now, deep tissue blood flow has been inaccessible to the optical method. Our laboratory has focussed on the development and application of diffuse correlation spectroscopy (DCS) for measurement of blood flow in deep tissues (for a recent review see [52]).

Speckle fluctuations of the diffuse light are sensitive to the motions of tissue scatterers such as red blood cells (Figure 5 (a)). The quantity containing this information is the electric field $E(\mathbf{r}, t)$. The electric field temporal autocorrelation function, $G_1(\mathbf{r}, \tau) = \langle E(\mathbf{r}, t)E^*(\mathbf{r}, t+\tau)\rangle$ is explicitly related to

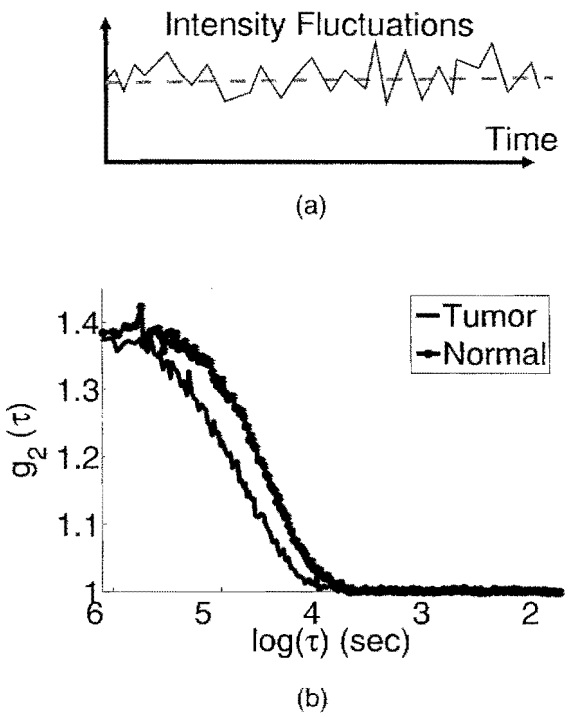

Figure 5. (a) The photons injected into the turbid medium undergo absorption and scattering, but the translational motion of the scatterers such as red blood cells leads to fluctuations in intensity. (b) Example of the temporal light intensity autocorrelation function, $g_2(\tau)$ measured in tumor (dark) and healthy (light) tissue from a subject with breast carcinoma. Faster decay corresponds to increased blood flow.

the motion of the scatterers. Here the angle brackets $\langle\rangle$ denote averages over time and τ is called the correlation delay time. The propagation of $G_1(\mathbf{r}, \tau)$ was originally described for colloidal turbid media using a diffusion model based on an integration over photon paths [157, 158]. A particularly useful result for the problem is the correlation diffusion equation [159–163] which is derived from P_1 approximation to the correlation transport equation [160, 161].

$$\nabla \cdot (D\nabla G_1(\mathbf{r}, \tau)) - \left(\mu_a + \frac{1}{3}\mu_s' k_0^2 \xi \langle \Delta r^2(\tau)\rangle\right) G_1(\mathbf{r}, \tau) = -S(\mathbf{r}). \tag{12}$$

where k_0 is the wavevector of the photons in the medium and $\langle \Delta r^2(\tau)\rangle$ is the mean-square displacement in time τ of the scattering particles. $S(\mathbf{r})$ is the source light distribution, and ξ is the ratio of the number of moving scatterers such as a red blood cell to the total number of scatterers (including static scatterers).

From the measured normalized intensity autocorrelation function, we derive the normalized diffuse electric field temporal autocorrelation function, $g_1(\mathbf{r}, \tau) = G_1(\mathbf{r}, \tau)/\langle |E|^2\rangle$. For the case of diffusive motion, $\langle \Delta r^2(\tau)\rangle = 6D_B\tau$, where D_B is an effective diffusion coefficient for the red blood cells. It should be noted that D_B need not (and is generally not) be the "thermal" Brownian motion predicted by Einstein;

nonthermal random forces in the vasculature can also give rise to diffusive particle motions. It is assumed herein that measured relative changes of ξD_B are proportional to relative changes in tissue blood flow.

A CW laser with a long coherence length and a single photon counting detector are needed for DCS measurements. An autocorrelator takes the detector output and uses photon arrival times to compute the light intensity autocorrelation function $g_2(\mathbf{r}, \tau)$ where it is linked to $g_1(\mathbf{r}, \tau)$ via the Sigert relation $g_2(\mathbf{r}, \tau) = 1 + \beta|g_1(\mathbf{r}, \tau)|^2$ [164]. An example of temporal light intensity autocorrelation function g_2 measured in tumor (dark) and healthy (light) tissue from a subject with breast carcinoma [165] is presented in Figure 5(b). Faster decay corresponds to increased blood flow.

3. INSTRUMENTATION

DOT/DOS instruments used for breast cancer applications can be roughly categorized by choice of light sources/detectors, measurement type (CW, FD, TD), and geometry (remission, rings, parallel-plate, etc). The choice of light sources, detectors, and measurement geometry determine the sensitivity of the instrument. The measurement types (described in Fig. 1) determine the light source modulation and detection techniques. The measurement geometry is defined by the positions of the light sources and detectors, which, in turn, influence the field of view for breast tissue.

Three types of light sources are used for DOS and DOT applications: white light, light emitting diodes, and laser diodes. Among these, laser diodes are the most popular because of their monochromatic nature. White light sources have gained more attention recently because the importance of multiple wavelength schemes has been recognized [69, 146]. The photodiode, the avalanche photodiode (APD), the photomultiplier tube (PMT), and the charge coupled device (CCD) are four detectors for DOT applications. The photodiode, even though it is a robust and inexpensive detector, is not used widely because it requires high light levels. The APD and the PMT are high-speed, highly sensitive detectors that are used widely for single-channel applications. The CCD, on the other hand, enables parallel detection at multiple spatial positions.

The detection electronics require extraction of intensity for CW, intensity and phase-shift for FD, and pulse shape for the TD technique. Schematics of some of this instrumentation are shown in Figure 6. The CW technique is the easiest and the most inexpensive of the three techniques per detector channel. This feature enables easy extension to many detector channels and, therefore provides substantial spatial information. Also, for a given source-detector separation, the CW technique enables deepest penetration into the tissue with good signal-to-noise. However, the information content per detector channel is the richest for the TD technique. Due to lack of information content, there have been concerns about the CW technique. In particular, absorption and scattering crosstalk in the images

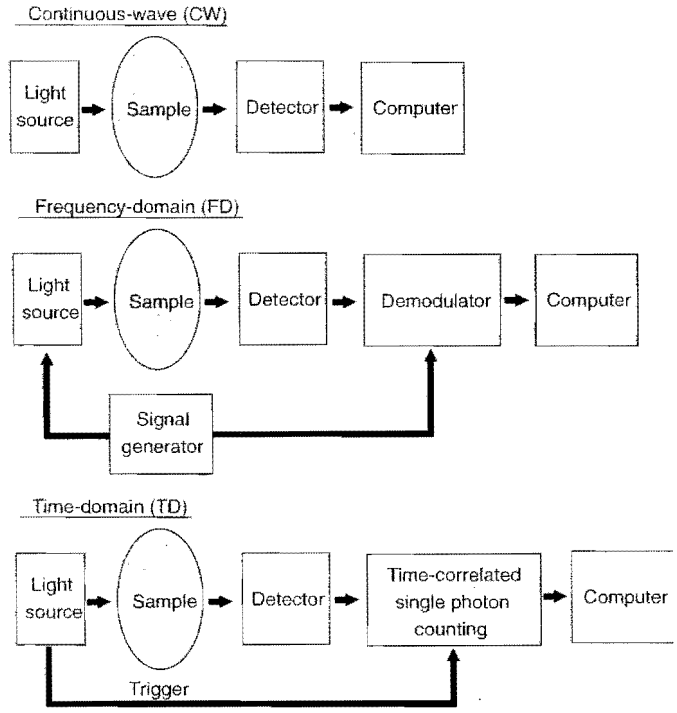

Figure 6. Schematics of instrumentation for CW, FD, and TD techniques. The detection electronics require extraction of intensity for CW, intensity and phase-shift for FD (using a demodulator [169]), and pulse shape for the TD technique (using time-correlated single photon counting [170]).

becomes an issue due to non-uniqueness considerations [166]. Barbour and co-workers [167] and Jiang and co-workers [168] formulated scaling approaches to circumvent this problem, and Corlu et al. [152, 154] have theoretically demonstrated that a successful separation of chromophore concentration and scattering is possible for the CW technique by using the multispectral method with optimal wavelengths.

The placement of light sources and detectors defines the measurement geometry (Fig. 7). In the remission geometry, light sources and detectors are placed in the same plane. Multiple scattering causes photons to deviate from the straight path and, therefore, reach the detectors placed in the same plane after traveling through the tissue below the source-detector pairs. In the parallel-plate design, *in vivo* tissue lies between two planes; light sources can reside in one plane and detectors in the other plane. The parallel-plate geometry has advantages in signal-to-noise (SNR) and ready detection by a lens-coupled CCD. The conical geometry (either made of multiple rings or conically shaped cup) has light sources and detectors surrounding the breast Thus, there is no loss of resolution in one direction, but the detectors need to have large dynamic range because some are very close to one another, whereas others are far apart.

Table 1 summarizes the instrumental features of most groups with *in vivo* breast cancer results. In the remission geometry, an analytic solution for the semi-infinite geometry is widely used to derive spectroscopic bulk properties [135,

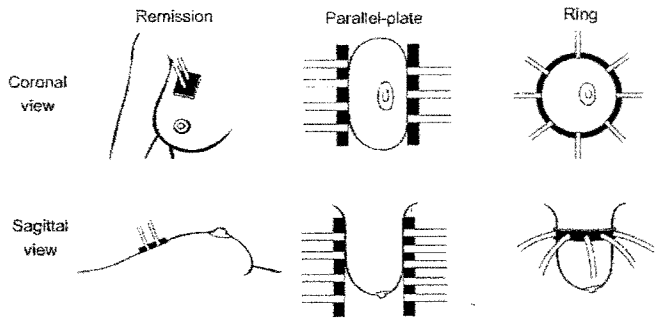

Figure 7. Measurement geometries for breast. In the remission geometry, light sources and detectors are placed in the same plane. In the parallel-plate geometry, light sources can reside in one plane and detectors in the other plane; the tissue lies in-between. In the ring geometry, light sources and detectors surround the breast.

146]. Barbour and co-workers [136] have developed a fast system that captures how breast cancer reacts to fast perturbations. Most of the European groups have utilized a tandem-style measurement in which light source and detector are placed directly across from one another at the shortest possible distance. These pairs are scanned across the whole breast. The primary weakness of this approach is that the measurement lacks off-axis projection. Recently, preliminary results are showing the usefulness of additional off-axis measurements [36, 144]. Several groups have explored co-registration with conventional imaging modalities such as ultrasound [139], MRI [26, 171], and X-ray [141]. Sevick-Muraca and co-workers have pioneered instrumental/theoretical aspects of fluorescence imaging using frequency-domain CCD detection. They have shown the feasibility of fluorescence DOT for realistic breast tissue phantom [172]. A combination of CW and FD techniques is utilized by many groups as the importance of multiple optodes and multiple wavelengths has been realized. Among these instruments, we will describe our DOT system in detail. A schematic of the DOT instrument is shown in Figure 8. The hybrid system combines frequency-domain (FD) remission and continuous-wave (CW) transmission detection. This parallel-plane DOT system has been extensively characterized for breast cancer imaging using tissue phantoms and a healthy female volunteer [147] and has been used extensively for breast cancer imaging [205].

The table was designed so that when the female subject lies on it in the prone position, both her breasts are inside a breast box (60 cm × 22 cm × 23 cm) underneath the table. A breast

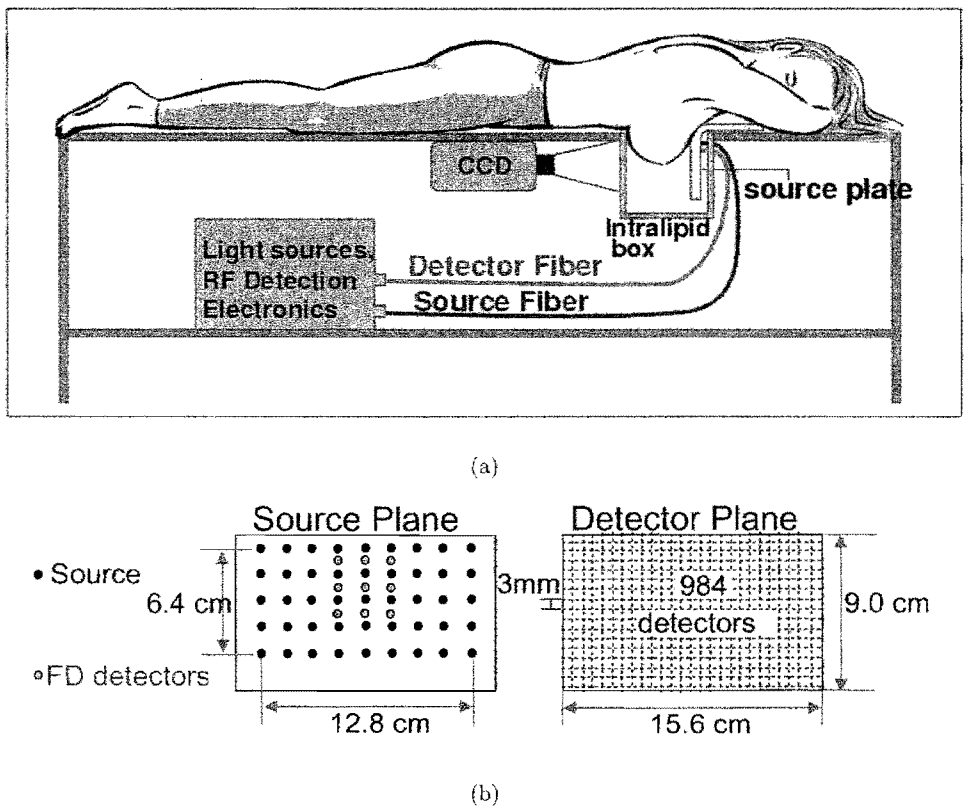

Figure 8. Schematic of parallel plate diffuse optical tomography instrument. (a) Frequency-domain (FD) remission and continuous-wave transmission measurements are performed simultaneously on a female subject lying in the prone position. (b) The source plate contains 45 source positions and 9 FD detectors. 984 detection points with 3 mm spacing are selected from CCD data for image reconstruction. Reprinted with permission from [34], R. Choe et al., *Med. Phys.*, 32:1128 (2005). © 2005, American Institute of Physics.

is typically centered and softly compressed between a movable compression plate and a parallel viewing window with cranio-caudal compression. The compression distance varied from 5.5 to 7.5 cm, depending on breast size. The breast box was then filled with the matching fluid that has optical properties similar to human tissue. The matching fluid was made with a scattering agent Liposyn III (30%, Abbott Laboratories, Chicago, IL), and an absorption agent India ink (Black India 4415, Sanford, Bellwood, IL). After the human subject measurements, reference optical measurements are performed on the box filled completely with matching fluid. For the reference measurements, a silicone (RTV12 with carbon black and TiO_2) block was placed on top of the box to extend the diffuse medium in a manner analogous to the subject's chestwall; this approach avoids signal saturation due to reflection from the air boundary.

Four laser diodes at 690, 750, 786 and 830 nm were sinusoidally intensity modulated at 70 MHz. The modulation depth for each wavelength was 86%, 99%, 72% and 67% respectively. 650 and 905 nm CW laser diodes have recently been added to the instrument. A combination of optical switches (DiCon Fiber Optics) was used for wavelength switching. The light output was relayed to a 1×48 switch (DiCon Fiber Optics, GP700) to access the various light source positions on the compression plate. The compression plate had 45 fibers in a 9×5 grid with a spacing of 1.6 cm (12.8 cm $\times$ 6.4 cm). The optical fibers embedded in the compression plate was of 200 μm diameter (FIS). Time-multiplexing was used for both wavelength and position switching. In particular, all wavelengths were multiplexed for each source position.

Nine 3 mm diameter fiber bundles were connected to the frequency-domain detection module and interlaced in a 3×3 grid on the compression plate as shown in Figure 8(b). A homodyne technique [169] was utilized to extract the amplitude and phase of the detected remission signal. The electrical signal from the avalanche photodiode (APD, Hamamatsu C5331-04) was amplified (Mini-Circuits ZFL-500LN, 24 dB), filtered by a band pass filter (Mini-Circuits BLP-70), and then amplified again (Mini-Circuits ZFL-500HLN, 19 dB). An I&Q demodulator (Mini- Circuits ZFMIQ-70D) with a series of low pass filters (Mini-Circuits SLP-1.9 and 100 Hz RC circuit) extracted the amplitude and phase by comparing the signal with the reference signal driving laser diodes [169]. The frequency-domain measurements were used for accurate quantification of bulk properties of human tissue and matching fluid, thus improving our initial guess for the image reconstruction. A lens-coupled 16-bit CCD camera system was used for collecting CW transmission data with an anti-reflection coated glass viewing window. A lens (Nikkor AF 50 mm F/1 .4D) relayed the detection plane (inner glass window in contact with breast) onto the CCD chip (2.68 $\times$ 2.6 cm). To reduce ambient light, a long-pass color-glass filter (630 mm, CVI Laser Inc.) was placed in front of the lens and a light shielding box was placed surrounding the space between the viewing window and the camera. A thermo-electrically cooled CCD pixel array (Roper Scientific, VersArray:1300, 1340 $\times$ 1300 pixel) was used for light detection, with a 1140 $\times$ 800 pixel region of interest (ROI) and 2 $\times$ 2 on-chip binning, resulting in a frame size of 570 $\times$ 400 pixels covering a detection area of 16 $\times$ 11 cm.

4. CLINICAL OBSERVATIONS

4.1. Endogenous Properties of Normal Breast Tissue

Thomsen & Tatman [22] have said, "to discover the abnormal, one first has to know the normal." A good understanding of normal breast optical properties is important for assessment of breast cancer signals. Recent spectroscopic research on normal tissues are providing more insight about their optically derived properties and the correlation of these properties with physiological parameters such as body mass index (BMI), age, breast thickness, radiographic density, parenchymal type, etc. [27, 33, 173–177].

An example of such study is from Durduran et al. [151] where the bulk optical properties (i.e. μ_a, μ_s', THC and StO_2) of 52 healthy female subjects were quantified. Significant intersubject variation is reflected in the Figure 9(a) with the mean THC of 34 ± 9 μM and the mean StO_2 of $68 \pm 8\%$. Among the demographic factors, an inverse correlation of THC and BMI (as shown in Figure 9(b)) and μ_s' and BMI (not shown) were observed. The physiological noise caused by averaged effects from heart rate, respiration, etc., were found to be of the order ~5% for THC and ~4% for StO_2 from the repeated measurements on the same breast [151].

Intersubject variation is caused by differences in the breast tissue composition of each individual, which is implied from the correlations with BMI and mammographic density. A significant inverse correlation between THC and BMI were found across a wide range of instrumentation and measurement geometries [36, 151, 174, 178]. Higher BMI is usually accompanied by more adipose tissue content wherein the blood supply is smaller than in glandular tissue [22]. Also, there is some inverse correlation between scattering and BMI [151] through the scatter power b (related to scatterer size) [36, 179]. Correlations with other parameters such as breast diameter [174] and breast thickness [36, 178] have been examined. Scattering prefactor and power were statistically different in the fatty category and the extremely dense category of radiographic density [174]. Further investigations using the mean particle size and number density based on measurements of μ_s' yielded results consistent with the microscopic characteristics of breasts categorized with radiographic density [180]. When the radiographic density were grouped into a low-density group and a high-density group, THC, scattering prefactor, and scattering power showed significant differences [181].

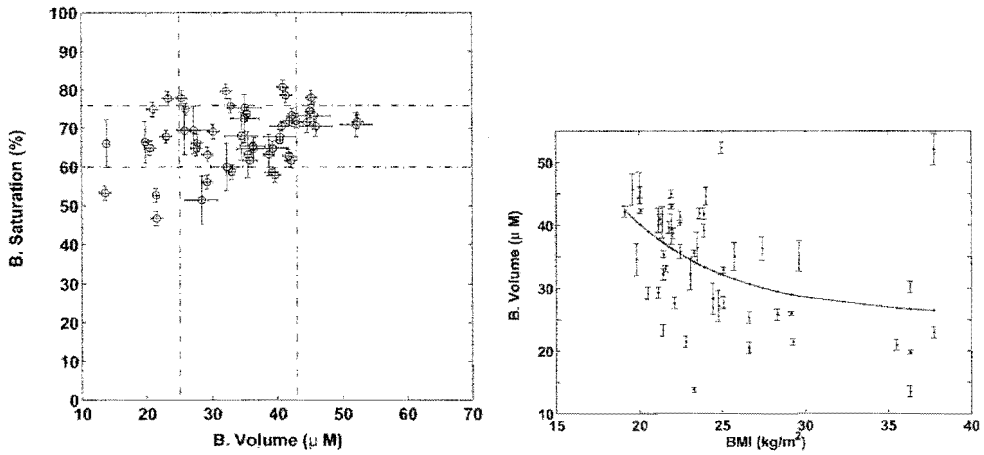

Figure 9. (a) Blood oxygen saturation (B. Saturation) vs total hemoglobin concentration (B. Volume) of breast tissue from 52 healthy subjects. The dashed lines indicate the standard deviation from the mean. (b) Total hemoglobin concentration vs BMI with a decaying exponential fit. Reprinted with permission from [151], Durduran et al., *Phys. Med. Biol.*, 47:2847 (2002). © 2002, IOP Publishing.

Mammographic parenchymal patterns can be derived from the X-ray attenuation characteristics of fat (radiolucent) and epithelial and stromal tissues (radiodense) [182]. Cubeddu and co-workers have found that water and lipid content correlated well with the mammographic parenchymal pattern, which is an indicator of the structural composition of adipose and fibrous tissue content [178]. The observation that optical measurements of absorption and scattering can provide physiologically relevant information about breast tissue composition [174] has been extended in a new direction by Lilge and co-workers. They assess breast cancer risk by comparing with mammographic parenchymal pattern [134, 183]. Based on parenchymal pattern classification studies, it was found that women with dense tissue in more than 60–75% of the breast are at four to six times greater risk of breast cancer than others [182]. Using a principal components analysis (PCA) of a broadband optical measurement, Lilge and co-workers have predicted the mammographic assessment of tissue density (high vs low) with 90% accuracy [134, 183].

Breast tissue composition can change significantly with age or hormonal status. Age-dependent studies have been carried out by several research groups. Some groups do not see much correlation with age [36, 151], whereas others have observed correlations with scatter power [174] and lipid content [178]. Distinctions seem to stand out when the population is grouped according to its hormonal status (i.e., pre-menopausal, post-menopausal, and post-menopausal with hormone replacement therapy) [184, 185]. The mean *THC* and water content are higher and the lipid content is lower in the pre-menopausal group [185]. This is likely due to the general increase in relative fat and fibrous stroma volumes after menopause [22]. On the other hand, the short-term hormonal effects have been observed to lead to changes of up to 13–30% in *THC* [181, 184] during menstruation.

Intrasubject variability was investigated using a hand-held probe with DOS data taken at five positions per breast. μ_a and μ_s' variation of 20–40% and 5–20% have been reported [185, 186]. These optical property heterogeneities translate roughly to 20% *THC* and 6% StO_2 variation [186]. Intrasubject and intersubject variability emphasize the importance of quantifying cancer properties with respect to surrounding normal tissue properties in addition to absolute terms.

4.2. Breast Cancer Detection and Characterization Based on Endogenous Contrast

Several research groups have recruited and presented *in vivo* human breast cancer cases. In this section, we will focus on results from stand-alone DOS/DOT to characterize breast cancer. The results will be grouped with respect to the measurement geometry and reconstruction dimension (i.e., bulk average, 2D, or 3D).

The simplest *in vivo* DOS measurements utilize CW hand-held instruments and rely on optical/physiological contrast between the cancer tissue and the contralateral breast [40, 135]. These measurements have demonstrated sensitivity higher than 90% and specificity ranging from 67–93%. Such single-point measurements, however, are susceptible to systematic errors that arise from changes in source-detector coupling due to tissue contact and asymmetry between the two breasts [185].

Tromberg and co-workers [27] overcome this problem using a broadband line-scanning DOS instrument rich in spectral information. The line-scan localizes the mass position by changes of physiological parameters near the mass. In a case study (N = 3) with a ductal carcinoma *in situ* (DCIS), an invasive ductal carcinoma (IDC), and a fibroadenoma, the

lesion absorption was found to be 1.25 to 3-fold higher than the normal breast tissue [27]. A broadband light source and several discrete FD sources enable reliable quantification of oxy-, deoxy-hemoglobin, water and lipid concentration as well as scattering prefactor and power. In recent studies, the group is attempting to derive one combinational parameter or "optical index" that maximizes the differentiation of normal, benign, and malignant breast tissues [187].

Hand-held probes provide access to masses near axillary or chest-wall positions, which are hard to reach with prone-position oriented imaging instruments. However, DOS measurements are more suitable for palpable masses located at greater depths below the tissue surface and in the supine position. It is easy to misjudge the line-scan direction if the lesion position is not well-known. Moreover, the detection limitation with respect to tumor depth has not been systematically explored as yet. To overcome the partial volume effect resulting from treating the medium as homogeneous and the human errors from hand-held probe, many groups have focused on the development of the imaging instrumentation and associated reconstruction algorithms.

Most European groups report parallel-plate frequency-domain or time-domain instruments operating in the tandem scanning scheme (i.e., a single source and detector pair is placed across the slab and scanned over the whole plate). While the tandem scan represents an improvement over spectroscopic devices, it does not produce enough information to enable robust 3D image reconstruction due to a limited range of projections. The scans were conducted in a fashion similar to X-ray mammography (e.g., cranio-caudal and mediolateral or oblique projections). A pilot study [24] demonstrated potential for optical mammography with enhanced image contrast using the edge effect correction. A method to enhance the cancer detectability using spatial second-derivative image processing and an oxygenation index was developed and demonstrated [188, 189]. European groups from Berlin and Milan have recruited a significant number of subjects with breast lesions and recently have quantified lesion optical/physiological properties. They have utilized two strategies for data analysis: (1) Assessment of cancer detection ability by examination of time-gated images that are relatively more or less sensitive to absorption and scattering depending on gate time, and (2) Quantification of breast cancer in terms of physiological properties (i.e., THC, StO_2, μ_s') using an analytic solution for a homogeneous slab with spherical heterogeneity [121]. Rinneberg and co-workers [37, 38, 143, 170, 190, 191] found tumor contrast with respect to normal tissue to be $r\mu_a \simeq 2, r\mu_s' \simeq 1$, and $rTHC > 1$ (where r indicates relative measure between tumor and normal, i.e. $r\mu_a = \mu_a^{tumor}/\mu_a^{normal}$) [191]. $rStO_2$ contrast was not observed. Cubeddu and co-workers [39, 142, 192–194] extended the spectral range by adding wavelengths longer than 900 nm to determine different lesion type by μ_a and μ_s' for 101 cases [193]. In this case, intensity images and scattering images were quantified directly rather than by fitting for chromophores. Cancers exhibited high μ_a at short wavelengths (where hemoglobin concentrations are high), cysts exhibited low μ_s' for all wavelengths, and fibroadenomas showed low μ_a at 913 nm and high μ_a at 975 nm. Recently, Rinneberg and co-workers have implemented off-axis measurements into tandem scanning configuration and demonstrated the ability to reconstruct μ_a and μ_s' images in three-dimension [144]. However, some blurring of μ_a occurred along the compression direction due to the limited angular range.

Experiments based on multiple ring and/or conical geometries have developed from 2D to 3D imaging. Pilot studies by Philips Corp. using a 256×256 CW instrument with matching fluid have been analyzed with the backprojection method and algebraic reconstruction technique to reconstruct three-dimensional images of the photon attenuation coefficient [25, 195]. Jiang and co-workers have demonstrated the three-dimensional DOT images of multiple carcinomas [29], but have, for the most part, concentrated on 2D images of μ_a and μ_s' to assess the differentiation of lesion types. Tumor was found to have higher μ_a and μ_s' at 785 nm, and fibroadenoma was found to have high μ_a and low μ_s' at 785 nm for nine lesions [196]. On the other hand, four of six cysts exhibited low μ_a and μ_s' [197]. Hebden and co-workers [198] have reconstructed the absorption of various lesions in 2D with some success using a ring-geometry time-domain instrument [198]. However, the rigid ring design made it difficult to accommodate some of the breast (especially with malignant lesions) and resulted in no image. Barbour and co-workers carried out a study in a bilateral conical geometry [35, 199]. They found tumor contrast in oxygen supply/demand imbalance and vasomotor response from Valsalva maneuver [35]. Pogue and co-workers [28, 155, 171, 200–202] have demonstrated reliable three-dimensional image reconstruction results based on ring geometry FD measurements via systematic tissue phantom studies and *in vivo* breast studies. While continuing to improve general quantification by the multi-spectral method [155] and the quantification of small objects [201], they are actively exploring the relationship between the microscopic and macroscopic optical contrast. They found a linear relationship between the blood vessel density measured by pathologic methods and the total hemoglobin concentration of breast cancer measured by DOT [28]. Their efforts to further improve quantification and explore new contrast mechanisms resulted in development of a broadband 3D imaging system, and video-rate imaging system [203]. To overcome resolution limitations of DOT, they have also started the co-registration with MRI [171, 202]. Preliminary results on healthy subjects showed higher water content, THC, and slightly lower StO_2 in fibroglandular tissue compared to adipose tissue.

An example of 3D reconstructed images using the ring geometry [204] is presented in Figure 10. The patient presented for standard screening mammography, which revealed a subtle

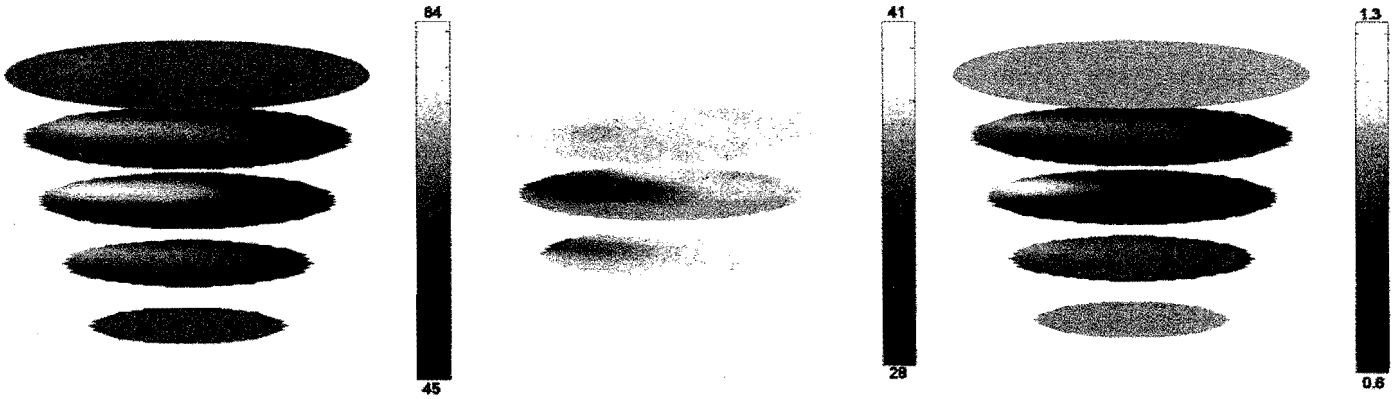

Figure 10. Reconstructed images of *THC* (μM), StO_2 (%), μ_s' at 785 nm (cm^{-1}) from a subject with an invasive carcinoma (9 o'clock). The images are coronal views of the cross-section through the breast, arranged from the bottom near the nipple to the top near the chest. Reprinted with permission from [204], H. Dehghani et al., in *Optical Tomography and Spectroscopy of Tissue V*, (Chance, Ed.), Vol. 4955, p. 191. Proceedings of SPIE, Bellingham, WA © 2003, The International Society for Optical Engineering.

nodular density and associated architectural distortion in the lateral side of the right breast. Pathology showed an invasive carcinoma of 20 mm size. The patient was presented for NIR measurements soon after biopsy. Among the reconstructed parameters, only *THC*, StO_2, and μ_s' at 785 nm are shown in Figure 10. Here the images are three-dimensional reconstructions and coronal slices at $z = -60, -45, -30, -15$ and 0 mm are shown. From the reconstructed images, it can be seen that an anomaly is found within the mid-plane at approximately the 9 o'clock position. The anomaly was associated with a *Hb* peak value of 47.7 μM, compared to a background of 32.9 μM, whereas the HbO_2 image presented a peak value of 24.7 μM at a location on the periphery of the skin (not shown). *THC* also presents a peak at the location of the anomaly, with a value of 65.3 μM (background value: 53.1 μM). StO_2 shows a marked decrease at the location of the anomaly, with a value of 25.9%, as compared to a background value of 38.1%. The μ_s' image presents an increase at the location of the anomaly. These trends are perhaps expected for a malignant tissue, as one would expect a rise in blood content, due to an increase in blood vessel density, but because malignant tumors are more active, there might also be a decrease in oxygen saturation.

Parallel-plate geometry instruments for 3D imaging are geared toward producing multiple off-axis projections by having multiple source positions and detector positions. As an example [205], three-dimensional images measured with our DOT instrument are shown in Figure 8. A 59-year-old female with invasive ductal carcinomas in her right breast is presented in Figure 12. She had two masses at 2 o'clock (2.0 cm) and at 10 o'clock detected by X-ray mammography, ultrasound, and MRI (See Fig. 11(a)). Ultrasound-guided core biopsy with a 15 gauge needle on a 10 o'clock mass was performed eight days before optical measurement, which found invasive ductal carcinoma with high-grade nuclei. During the DOT measurement, a bruise due to recent core biopsy was observed in the lower outer quadrant surface of the right breast. (See bottom part of Fig. 11(a)).

The three-dimensional images of this patient were reconstructed from the data using nonlinear 3D reconstruction algorithms that incorporated the multi-spectral method with envelope-guided spatially variant reconstruction [154]. Geometric constraints were further used to segment the problem into a breast region and a matching fluid region. For the initial guess, C_{Hb}, C_{HbO_2}, and A were assigned to the breast and the matching fluid based on the bulk measurements. The 3D images are presented in a manner similar to that of Figure 11(b). Each slice represents a 16 × 11 cm image in x–z plane, with the caudal-cranial view (i.e., from feet to head, same as the CCD camera view). The orientation of each image is such that the right side of the image slice is lateral (toward the outer side of breast) and left side is medial (toward the middle of the breasts) for the right breast, and vice versa for the left-breast. For convenience of presentation, slices at selected spatial intervals are presented. Because the reconstructed data on FEM nodes is interpolated to a regular grid of 0.2 cm spacing, each slice has 0.2 cm of pixel size in the x and z directions.

In *THC* and μ_s', images (Fig. 12), two distinct enhancements corresponding to 2 and 10 o'clock are observed at distinct locations in three-dimensions. The extension of 10 o'clock enhancement through the middle sections in the y direction could be attributed to the bruise effect induced by core biopsy. An interesting distribution of StO_2 is noticeable where the biopsied area near the detection plane has much lower oxygen saturation.

The tumor contrasts ($rTHC$, $r\mu_s'$, $rStO_2$) from 21 subjects [205] with carcinomas are plotted in a bar graph in Figure 13. First, an average ($\bar{p}$) and a standard deviation (σ_p) was calculated for *THC*, StO_2, and μ_s' in each image. Then the tumor region was defined by $p > \bar{p} + 2 \times \sigma_p$, because values greater than $2 \times \sigma_p$ have a 95% chance to be different from the average with the assumption of a gaussian distribution.

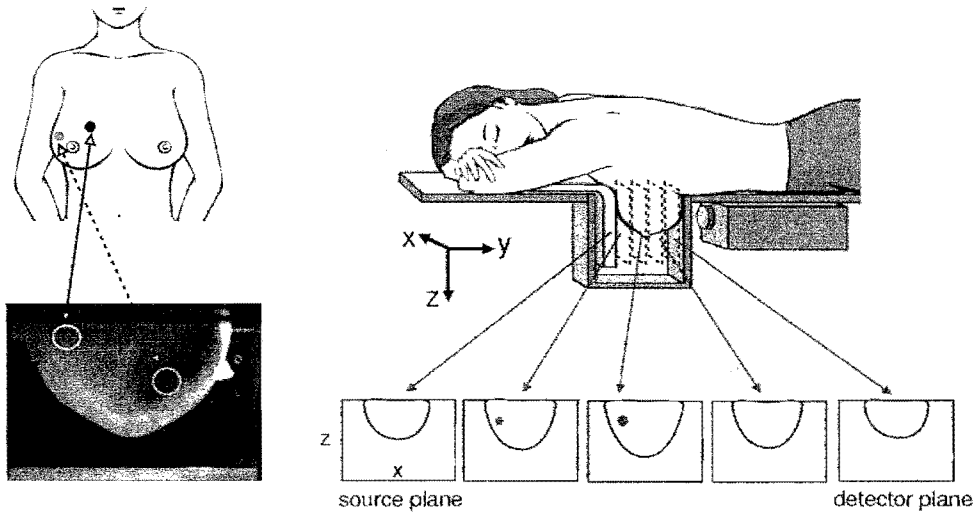

(a) (b)

Figure 11. (a) The multiple lesion (2 o'clock and 10 o'clock) locations in frontal view (top) and in caudal- cranial view photo (bottom) of a subject with the DOT image reconstruction in Figure 12. Note the bruise on the breast surface due to previous core biopsy (bottom), (b) The orientation of reconstructed 3D images. Each slice is in caudal-cranial view, where the left side is medial and the right side is lateral for the right breast. For simplicity, only selected slices from y direction will be presented, starting from the head on the left side to the feet on the right side.

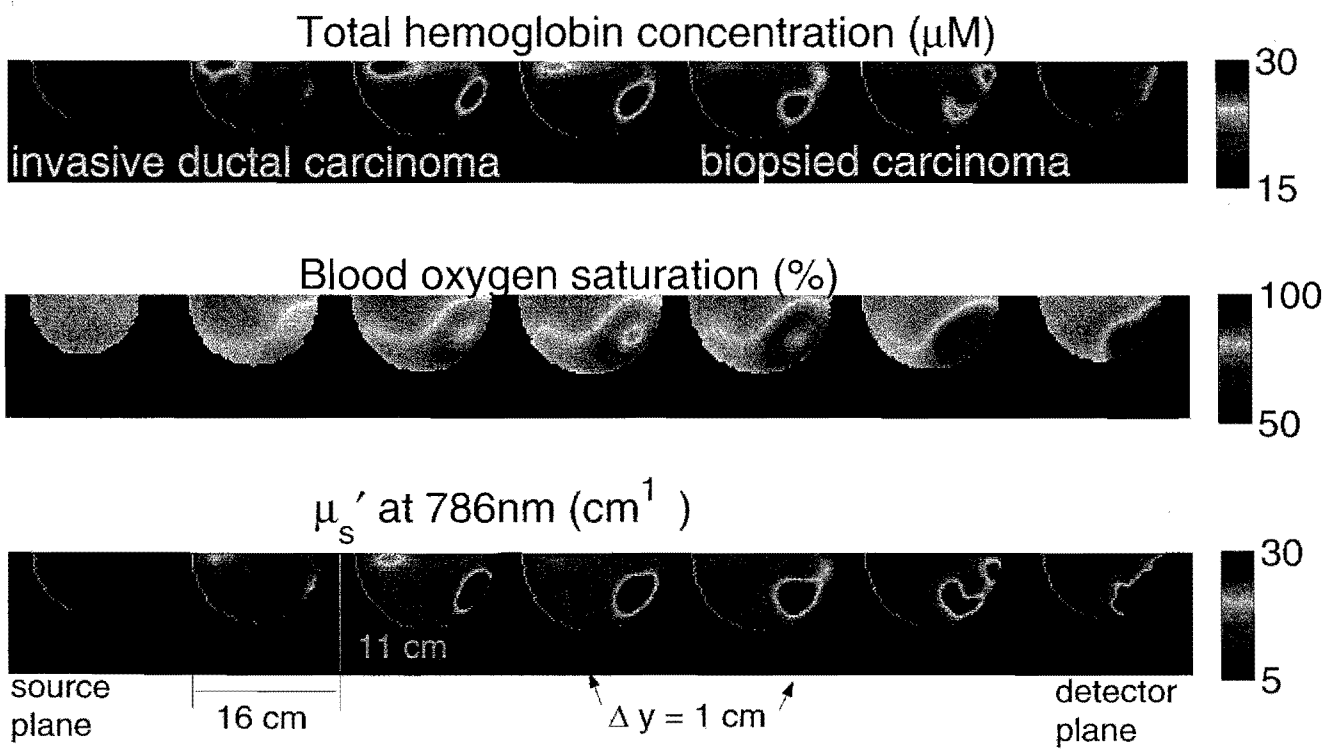

Figure 12. 3D reconstructed images of THC, StO_2, and μ_s' at 786 nm of a subject with multiple ductal carcinomas in her right breast. Two invasive ductal carcinomas show an increase of THC and μ_s' compared to the surrounding tissue. The location of the two lesions is differentiable in three-dimension. The dramatic decrease of StO_2 related with the bruise from the core biopsy appears in the slices near the detector plane.

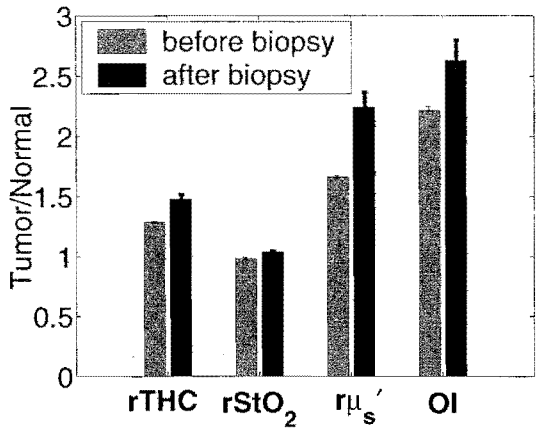

Figure 13. Tumor contrast from 22 carcinomas. *rTHC*, $rStO_2$ and $r\mu_s'$ are the relative ratio between tumor and normal. *OI* is an optical index defined as $\frac{rTHC \cdot r\mu_s'}{rStO_2}$. Light gray bars are from DOT measurements before core biopsy (N = 14), and dark gray bars are from after core biopsy (N = 8).

For StO_2, the threshold of $p < \bar{p} - 2 \times \sigma_p$ was considered based on tumor hypoxia hypothesis; this did not yield any tumor region. Tumor regions estimated from *THC* and μ_s' were averaged to define the average tumor region. Relative *THC* ($rTHC = THC_{tumor}/THC_{normal}$) was calculated by averaging *THC* in the tumor region and outside the tumor region as defined above. Relative μ_s' and relative StO_2 were defined in the same way. *rTHC* error bars were estimated based on standard deviation of THC_{tumor} and THC_{normal}. Relative μ_s', ($r\mu_s'$) and relative StO_2 ($rStO_2$) error bars were defined in the same way. Note that $rStO_2$ is around 1 and does not vary much. We define an optical index (*OI*), which is a combination of the tumor contrast: $OI = \frac{rTHC \cdot r\mu_s'}{rStO_2}$. Optical indices such as this enables us to explore the possibility of maximizing optical contrast with a combination of variables. The combined contrast index *OI* was 2.63 ± 0.29.

Recently, Intes and co-workers [36] have quantified tumor contrast for 23 subjects, finding *rHb* is significantly greater in malignant than benign lesions. Their time-domain instrument consists of 1520 spatial detection points with on- and off-axis measurements at 4 wavelength (760–850 nm range) in parallel plate geometry with matching fluid.

High *THC* contrast of tumor has also been reported by other groups [28, 29, 32, 33, 196, 200, 206, 207] and has been supported by histopathologic analysis of microvessel density counts [28, 106]. The origin of scattering contrast is still illusive because careful comparable histopathologic analysis has not been done for scattering contrast and also because of absorption and scattering crosstalk issues. Nevertheless, the hypothesis that the increased number of scattering organelle due to proliferation of cells and the increased fibrosis should increase scattering support our findings. Some groups also see scattering contrast (~20%) [38, 200], but not to the extent found in our work. With respect to StO_2 contrast, there appears to be varying results; some groups observed a decrease of StO_2 in the tumor [27, 189, 190, 208], whereas others observed no difference [34, 209] or even an increase [200]. It may be possible that oxygen metabolism of cancer could be different depending on the stage and biochemical pathways involved.

These differences may arise from differences in instrumentation and reconstruction algorithm as well as from physiological inter-patient variation. *THC* emerged as robust quantity for the tumor contrast, but it is weak on its own for differentiation of malignancy. It is therefore important to find tissue optical indices that maximize the malignancy contrast and are independent of instrument, reconstruction scheme, and parameter crosstalk. The field is still evolving to devise the instrument and reconstruction algorithm to improve accuracy (via multiple spectral and spatial information) and are gathering more statistics.

4.3. Blood Flow in Breast Cancer

Blood flow in breast cancer potentially provides a novel contrast over methods that measure essentially tumor morphology. Some capability for tumor differentiation based on blood flow was demonstrated already by ultrasound and MRI [210–213]. Therefore, we expect that diffuse optical blood flow measurements will be of value because the instruments are inexpensive, portable, and the signals are robust. It is further known that the metabolic changes due to cancer therapy can precede size changes accessible to traditional imaging or clinical palpation methods [214]. Diffuse correlation spectroscopy (DCS) for measurement of tissue blood flow [52, 111] can be readily combined with DOS for measurement of tissue blood oxygenation to calculate oxygen metabolism in tumors or changes thereafter.

Previous attempts to measure blood flow in the breast have been carried out using Positron Emission Tomography (PET) [215–217], color and power Doppler ultrasound [210, 218, 219], and MRI [211]. PET studies were limited in extent, but have shown that blood flow tends to increase in malignant tumors. Ultrasound techniques, on the other hand, were used from the late 1980s to 1990s, but the clinical utility of the technique was not established. PET was limited because of its cost and availability, whereas ultrasound techniques had poor signal-to-noise and low contrast. Ultrasound techniques are also biased toward large vessels and, therefore, are susceptible to issues such as arterio-venous shunting. MRI studies require high-cost, low-throughput research instrumentation and are limited by signal-to-noise.

Recently we have explored these issues with DCS [165]. To this end, we recruited three subjects with palpable tumors, two subjects with mammographically identified calcification, and two healthy subjects. The measurements were carried out at the Hospital of the University of Pennsylvania and were

approved by the Internal Review Board. Subjects were asked to lay back in the supine position, thus flattening the breast and increasing tumor accessibility. A hand-held probe was scanned in horizontal and vertical directions in 2 cm increments across the tumor. In the case of healthy volunteers, an arbitrary region was drawn as the tumor site and a measurement was obtained by scanning across that region; this provided a measure of the heterogeneity of blood flow. Average optical properties necessary for analysis were obtained from separate DOS measurements of the same patients [34].

Details of the instrument are described elsewhere [52, 165]. A complete set of data was acquired every six seconds and five such sets were acquired at each position. For this study, we recorded data for each of the four source-detector positions directly across from each other (separation of 2.5 cm) at each scanned position. The recorded correlation functions were then fit to a solution of the diffuse photon correlation equation [52] to obtain an index proportional to the blood flow. The results are normalized to the mean value of the measurements of the healthy tissue and the standard deviation is reported as the error bar. We, therefore, report the averaged relative blood flow (% *rBF*) at each position.

Figure 5(b) shows two correlation curves from a patient with a malignant cancer. When blood flow increases, the temporal autocorrelation function decays more rapidly. It is evident that the blood flow is larger in the tumor region (compare dark and light curves) in both cases. Figure 14 shows horizontal and vertical profiles from one malignant tumor and one healthy breast. There is very little variation observable in the healthy breast, whereas the blood flow increased in both directions over the tumor indicating that the observed contrast is due to the tumor and not the natural heterogeneity of the breast.

To quantify the blood flow change in the tumors, we have used the estimated tumor outline and tabulated the standard ($\pm$ mean deviation) *rBF* in that region. Table 2 shows the distribution of the values for all subjects. Three groups are visible; (1) there is very little heterogeneity in the healthy breast (2.7% variation), (2) the blood flow of malignant tumors is increased to 230% of healthy tissue, whereas, (3) there is only a moderate increase in benign tumors (to 153%). Although, the power of the statistics of this study is not enough to conclusively claim differentiation, we note that these results are in qualitative agreement with previous Doppler ultrasound and PET results [210, 215–219] wherein ~ 470–550% increases in blood flow were reported in malignant tumors with smaller contrast in benign cases. In studies with larger populations, blood flow indices were used to differentiate up to nine different types of breast diseases [210].

These findings clearly demonstrate an ability to detect optically robust changes in blood flow in palpable tumors. Further studies with more source-detector pairs are now being undertaken to analyze potential partial volume effects that may influence our results. We note that these palpable tumors are relatively superficial, and previous optical studies [33, 220] have shown that source detector separations around 2.5 cm can

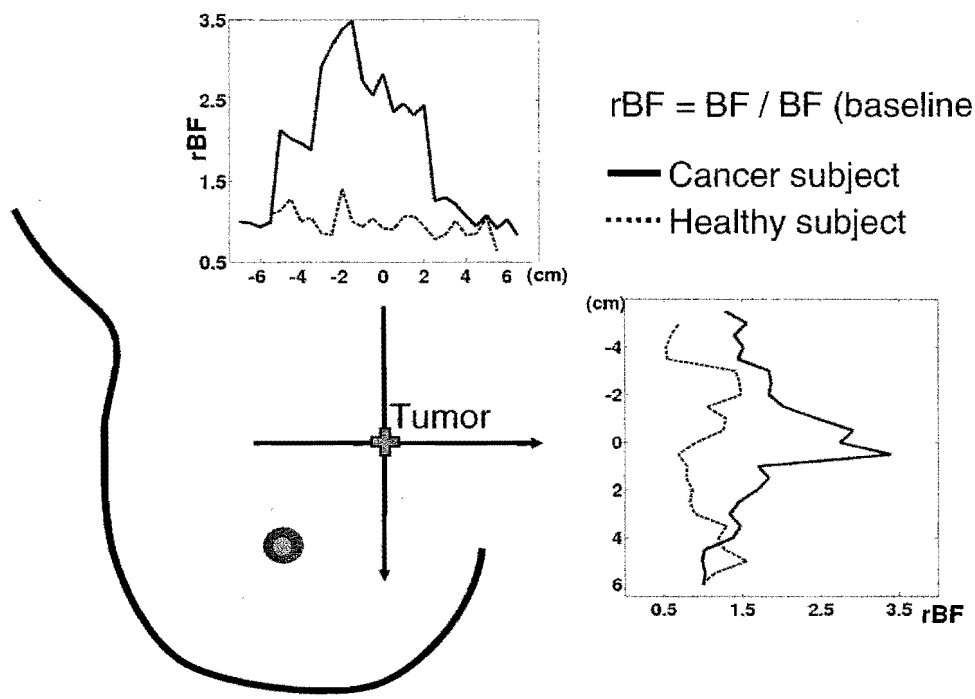

Figure 14. Relative blood flow (*rBF*) scans from one patient with a malignant tumor and a healthy volunteer are shown for both horizontal and vertical scans.

Table 2. Tabulation of relative blood flow (*rBF*) measured at the estimated tumor regions from all subjects grouped as healthy, benign, and with malignant disease.

Group	Type	*rBF* (± std) (%)
1	healthy	100.5 ± 13.4
1	healthy	105 ± 86
2	benign	144 ± 21
2	benign	163 ± 26
3	malignant	184 ± NA
3	malignant	212 ± 98
3	malignant	298 ± 51

effectively probe them in a repeatable manner. Additionally, if we assume that the palpable region corresponds to roughly the same depth from the skin, the partial volume effects are further divided out by normalizing to the healthy tissue blood flow. In the future, we will acquire data with a hybrid instrument [52] to measure the oxygenation and total hemoglobin concentration changes simultaneously and estimate the changes in oxygen metabolism of the tumors. The instruments are built on small clinical carts, and the study time is relatively short (~10 minutes). Therefore, it is feasible to acquire data at each patient visit and in the triage area. We anticipate these methods may become clinically useful for therapy monitoring and dose-adjustment.

4.4. Neoadjuvant Chemotherapy Monitoring

Information about tumor response during therapy is useful for treatment optimization. Early assessment of therapy efficacy, for example, is important for certain therapies and may only be effective for some of these. Non-responders may be losing valuable time waiting for adequate responses. Studies by PET suggest that physiological changes due to cancer therapy may occur earlier than the anatomical changes detectable by other imaging modalities [221].

DOT is especially attractive for therapy monitoring because it is noninvasive and inexpensive, and it lends itself to frequent monitoring (e.g., daily or hourly). Furthermore, DOT gives direct information about physiological parameters such as *THC* and StO_2. Indeed, a reduction of tumor angiogenesis from neoadjuvant chemotherapy in combination with hormone therapy has been confirmed by pathologic analysis [222]. The monitoring capability of DOS/DOT has been demonstrated for some cancer therapies in animal models [223] and in *in vivo* head and neck cancer [70]. For the *in vivo* breast cancer case, the utility of DOT has been demonstrated with success for neoadjuvant chemotherapy [33, 34, 106]. Also, an interesting case of monitoring interstitial laser photocoagulation (treatment option for fibroadenoma) was reported [224]. In this section, we will describe neoadjuvant chemotherapy monitoring using case studies from DOS [33] and DOT [34].

Neoadjuvant chemotherapy (i.e., pre-operative chemotherapy) is an important therapeutic approach for women with locally advanced breast cancer. If the patient responds to neoadjuvant chemotherapy, the size of the primary tumor decreases, facilitating better control through surgery while potentially eradicating micro-metastatic disease [225]. Neoadjuvant chemotherapy enables a higher percentage of patients to undergo breast conservation therapy without negatively impacting local recurrence rates or long-term outcome when compared with adjuvant chemotherapy [226]. Additionally, the neoadjuvant setting provides a means to monitor the effectiveness of chemotherapy by observing its effects on the primary tumor *in vivo*.

Widely used clinical methods are physical examination, mammographic and ultrasonographic evaluations which sometimes have limited utility for assessing tumor response due to chemotherapy-induced fibrosis [227–229]. MRI has proved useful for defining the extent of residual disease when compared with pathology [230, 231]. Also, dynamic contrast-enhanced magnetic resonance imaging (DCE-MRI) has demonstrated the ability to monitor tumor size and vascularity during neoadjuvant chemotherapy using gadolinium contrast agents [231–233]. The high cost of MRI, however, make it impractical for daily monitoring.

Jakubowski et al. [33] used a hand-held noninvasive DOS instrument to monitor a post-menopausal woman undergoing neoadjuvant chemotherapy. The combination of measurements by a CW spectrophotometer and a frequency-domain instrument (based on network analyzer) enabled acquisition of broadband NIR absorption spectra as well as μ_a and μ_s' at discrete wavelengths (10 wavelengths in 660–973 nm range). The probe consists of fibers connected to a white-light source and spectrophotometer pair and a laser source and APD pair at source-detector separation of 26 mm. (APD is directly coupled to the probe.)

Figure 15 summarizes results from a study of a 54-year-old post-menopausal Caucasian female with 2.4 × 2.5 × 2.2 cm high-grade intraductal carcinoma. The patient went through neoadjuvant chemotherapy spanning 68 days and three doxorubicin-cyclophosphamide (*AC*) cycles. She was recruited for the DOS measurement prior to the chemotherapy, daily at days 3–7, and at days 21, 24, 26, 28, 68. For each day, the patient was positioned supine at 30 degrees elevation. DOS measurements were performed at 17 locations across the tumor: two linear scans in medial-lateral direction and in cranial-caudal direction at 1 cm intervals.

Prior to the treatment, DOS results showed tumor-to-normal tissue contrast, *rTHC* to be 2.4, rH_2O (water fraction ratio) 6.9, $rStO_2$ 0.9 and rC_{lipid} (lipid fraction ratio) of 0.7. After completion of treatment, *rTHC* of 1.5, rH_2O of 2.1, $rStO_2$ of 1.4 and rC_{lipid} of 0.9 were found. Figure 15 shows the decrease of *THC* and water fraction with the progress of the treatment. A systemic drop in *THC* was observed in the

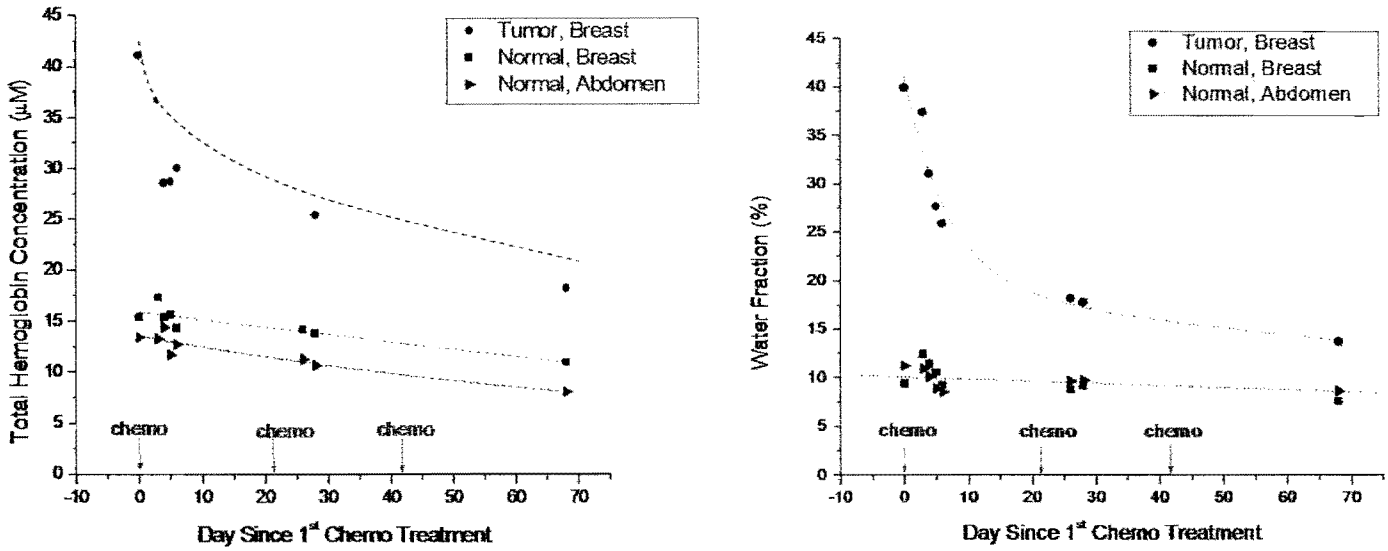

Figure 15. (a) Total hemoglobin concentration vs number of days since the first chemotherapy. *THC* maxima located over the tumor (dark circle), and control values from the abdomen (triangle) and normal part of breast (light square) are plotted. Although *THC* at the tumor site consistently fall, control values also decrease. (b) Water volume fraction vs number of days since the first chemotherapy. Water volume maxima located over the tumor and control values from the abdomen and breast are plotted. Water fraction in tumor falls rapidly, whereas control tissues maintain constant levels. Reprinted with permission from [33], D. B. Jakubowski et al., *J. Biomed. Opt.*, 9:230 (2004). © 2004. The Internal Society for Optical Engineering in cooperation with the International Biomedical Optics Society.

abdomen and normal breast in addition to the tumor (Fig. 15(a)), although with a different rate. This decreasing trend correlated with the steady decrease of blood hematocrit levels during the treatment period. However, the water fraction of normal breast and abdomen did not change with treatment. From the figure, one can note that approximately half of the *THC* and water fraction changes occurred within five days of treatment.

The monitoring capability in DOT imaging was demonstrated by Choe et al. [34] and compared with DCE-MRI. For this study, the parallel-plate DOT instrument described in Figure 8 was used.

A 35-year-old pre-menopausal Caucasian female with $5.3 \times 2.2 \times 2.7$ cm size invasive ductal carcinoma underwent neoadjuvant chemotherapy. The therapy consisted of four *AC* cycles followed by four Taxotere cycles at three weeks intervals. DCE-MRI measurements were, performed at the following time points: one week before chemotherapy (pre-chemotherapy); week 12 following completion of *AC*, but prior to initiation of Taxotere therapy, and week 23 following the completion of Taxotere therapy, but prior to surgical tumor removal (mastectomy). DOT measurements were performed at 10, 14, and 19 weeks after the first *AC* cycle (corresponding to after fourth, fifth, and seventh chemotherapy respectively).

Three-dimensional DOT images of *THC*, μ_s' at 786 nm and StO_2 were reconstructed. Reconstructed *THC* images after the fourth, fifth, and seventh chemotherapy are shown from top to bottom in Figure 16. In the *THC* images after the fourth chemotherapy cycle, a high *THC* region is found in slices near the source plane (1–3 cm deep from surface) and near the upper central part of the breast. After the fifth chemotherapy cycle, the tumor region is still identified by *THC* contrast near the source plane and in the upper central region. However, the contrasted region appears smaller than the corresponding region after the fourth chemotherapy cycle. The *THC* distribution after the seventh chemotherapy cycle is more homogeneous throughout the slices compared to previous chemotherapy cycles. Within the original tumor margins, the high *THC* region shifts toward outside of the tumor, leaving a relatively low *THC* region occupying most of the tumor extent. The fluctuation of average *THC* correlated well with hematocrit levels. μ_s' images (partially shown in Fig. 17) exhibits a similar trend, i.e., higher μ_s' values in the tumor region, and this region with high μ_s' shrinks over the course of treatment. However, StO_2 images (partially shown in Fig. 17) were relatively homogeneous and do not show contrast in the tumor region (i.e., not exceeding $2 \times \sigma_p$). Note, however, the overall StO_2 value decreased significantly after the fifth chemotherapy cycle and remained constant thereafter.

In rows of Figure 17, image slices corresponding to the cancer center (determined by maximum enhancement due to gadolinium uptake) are shown as MRI sagittal view, MRI axial view, DOT axial view of *THC*, StO_2, and μ_s' at 786 nm. They are arranged with respect to the measurement time points as columns. MRI images projected in sagittal and axial views are shown for the pre-chemotherapy point, after *AC* therapy (week 12) and after Taxotere therapy (week 23). The

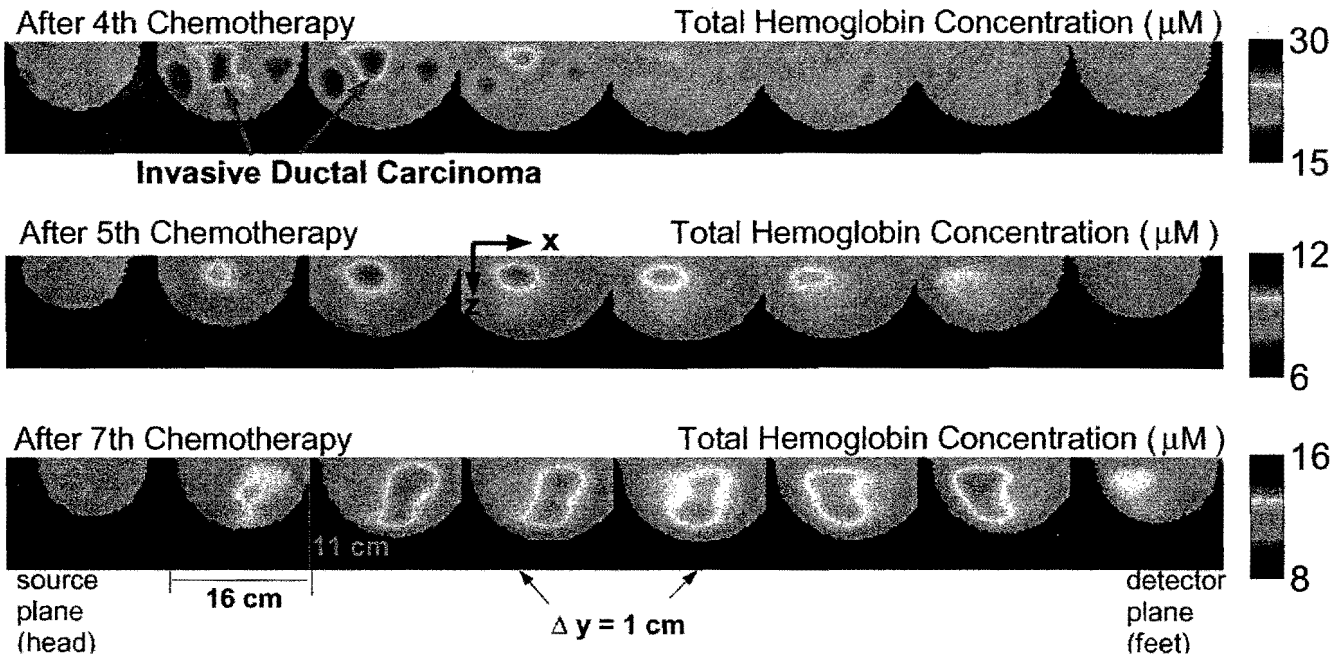

Figure 16. Three-dimensional reconstructed total hemoglobin concentration images. Image slices from source to detection plane are presented at 1 cm intervals in caudal-cranial view, from left to right. DOT images corresponding to after fourth, fifth and seventh chemotherapy were arranged from top to bottom. Reprinted with permission from [34], R. Choe et al., *Med. Phys.*, 32:1128 (2005). © 2005, American Institute of Physics.

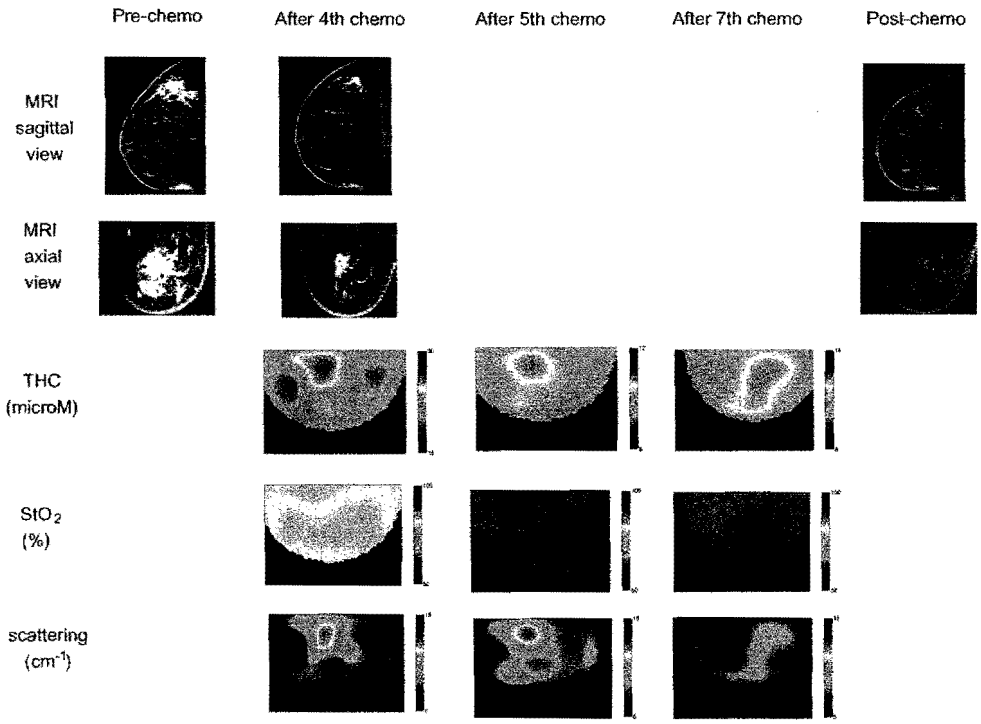

Figure 17. Representative image slices from MRI and DOT of the cancer. Dynamic contrast-enhanced MRI shows enhancement of gadolinium in the upper central quadrant of the breast at the pre-chemotherapy time point. The consistent shrinkage of the lesion is observed at after fourth chemotherapy and post-chemotherapy time points. Representative axial image slice of THC, StO_2 and μ_s' at 786 nm images from DOT are presented at after fourth, fifth and seventh chemotherapy time points. The shrinkage of the cancer is clearly shown in THC and μ_s' images. There is a significant decrease of overall StO_2 level between after fourth and fifth time points.

intensity of the DCE-MRI image is higher in the tumor due to increased tumor vascularity and gadolinium contrast uptake. Before chemotherapy, the tumor is clearly seen around 12 o'clock to 1 o'clock (upper quadrant in sagittal view, near center in axial view). After completion of chemotherapy cycles, the size and intensity of the enhancing region decreased significantly. Upon completion of chemotherapy, MRI demonstrated an amorphous 5–6 cm non-enhancing soft tissue region with only a scattered punctate form of enhancement. Pathology analysis done at mastectomy revealed the presence of residual infiltrating ductal carcinoma of size $1.5 \times 1.5 \times 0.7$ cm^3 at about the 1 o'clock position with intermediate grade nuclei, along with dense fibrosis and inflammation consistent with tumor response to chemotherapy.

In both MRI and DOT, the tumor was found in 12 o'clock, many centimeters away from the nipple. Also, there is a general trend of decreasing tumor volume in MRI and DOT respectively. More interestingly, DOT can provide direct information about relative *THC* between cancer and normal tissue (*rTHC*). Significant decreases of *rTHC* along with tumor shrinkage were observed after the fifth chemotherapy cycle, which is the first Taxotere chemotherapy. The *rTHC* after fifth and seventh chemotherapy cycles are equivalent, but accompanied with significant tumor volume decrease, implying tumor neovasculature regression with chemotherapy. The localized changes of these physiological parameters over time clearly demonstrate the dynamic imaging capability of the DOT method. The carcinoma cells in the post-chemotherapy stage were finely and diffusely dispersed in fibrous connective tissue, which represented the bulk of the residual mass. This remaining viable tumor was detected by MRI as focal enhancements and by DOT as small, but positive, *THC* contrast.

From these two cases studies, it is demonstrated that the physiological parameters measurable by DOS/DOT have potential to monitor tumor response to the cancer therapy and, furthermore, to predict early therapeutic responses. Further studies with a statistically significant subject number would be necessary to assess the full capacity of DOS/DOT in monitoring breast cancer therapy.

4.5. Co-registration with Other Modalities and Exogenous Contrast Agents

Several groups have now begun incorporating optical techniques with other imaging modalities. This approach can potentially overcome the resolution limitation problem of DOT by using spatial information provided by other imaging modalities as inverse problem constraints. Also, this approach provides extra physiological information to the other imaging modalities. One of the earliest attempts to combine with other imaging modalities was conducted using an exogenous contrast agent. Ntziachristos et al. [26, 234] combined time-domain DOT with MRI in a soft parallel-plate compressed breast geometry. Their most important contribution was the simultaneous direct verification of tumors by both techniques and the study of differential uptake of contrast agents in malignant tumors. More groups have begun to incorporate endogenous DOT into the MRI environment to utilize the high spatial resolution information from MRI to constrain DOT for better quantification [171, 235, 236]. Also, many have started combining information provided by MRI (not taken concurrently with DOT) to correlate with DOS/DOT results or to use as spatial constraints [34, 237].

Boas and co-workers [31] have co-registered DOT with 3D X-ray mammography in a hard compression instrument. Thus far, they have shown that *a priori* spatial information from a co-registered X-ray mammography can constrain DOT regularization in reconstruction of μ_a at 780 nm. There are some concerns that hard compression may reduce the hemodynamic tumor signatures. Indeed, preliminary *in vivo* results showed much smaller tumor contrast compared to other groups [141]. However, this approach will be interesting in the future.

There has also been research, combining ultrasound with optical methods, e.g., Holboke et al. [239], and Zhu et al. [32, 207, 238, 240]. The DOT problem in this case is made more difficult by the remission geometry and by poor definition of breast boundaries compared to other instruments. Nevertheless, Zhu and co-workers have constructed 3D DOT total hemoglobin concentration maps (assuming only absorption perturbation), identifying an *in situ* ductal carcinoma (N = 1) [207]; and in other studies they have distinguished early-stage invasive carcinomas (N = 2) from benign lesions (N = 17) [32].

In a different vein, DOT can be conducted with injection of exogenous contrast agent. Currently, Indocyanine Green (ICG) is the only FDA-approved compound suitable for DOT, having an absorption and fluorescence spectra in the NIR window. ICG was utilized to enhance absorption in case of DOT [26, 234]. Intes et al. [241] examined the *in vivo* uptake dynamics of ICG for three subjects and found somewhat different behaviors between benign and malignant tumors. Malignant cancers exhibited slower ICG washout rates than benign fibroadenoma, possibly due to leakiness of the blood vessels.

Sevick-Muraca and co-workers have been working on fluorescence DOT imaging using ICG [172, 242]. They have demonstrated that the ICG fluorescence signal is detectable in canine breast cancer by using plane-wave illumination in the frequency domain. In this case, back-reflected diffuse light was measured using an intensified CCD camera [242], thus attesting to the feasibility of the fluorescent contrast agent approach. Recently, 3D DOT fluorescence imaging in realistic breast phantoms has been accomplished [172]; this may be important for future studies with contrast agents and optical techniques.

These advances in diffuse optical tomography of the breast are critical for exploitation of the advances of molecular imaging [243–245], an emerging field of medicine with a promise of new generation optical contrast agents.

5. SUMMARY

The most effective clinical role for diffuse optical tomography (DOT) in the screening, diagnosis, and treatment monitoring of breast cancer has yet to be determined. It is clear, however, that DOT provides exquisite functional information directly related to tumor patho-physiology (e.g., metabolic activity, angiogenesis, and blood flow/concentration), and complementary to structural and functional information provided by conventional imaging. Furthermore, advances in diffuse optical tomography of the breast are critical for exploitation of the advances of molecular imaging [243–245], an emerging field of medicine with promise of a new generation of optical contrast agents.

ACKNOWLEDGMENTS

We have many colleagues and collaborators to thank for their contribution to this chapter. In particular, we thank Turgut Durduran and Alper Corlu for significant assistance in the preparation of this chapter. For other useful discussions over many years, we thank Joseph P. Culver, Britton Chance, Simon R. Arridge, Martin Schweiger, Kijoon Lee, Soren D. Konecky, Chao Zhou, Guoqiang Yu, David R. Busch, Ulas Sunar, Hsing-wen Wang, Jonathan A. N. Fisher, Monica J. Holboke, Leonid Zubkov, Joseph M. Giammarco, David A. Boas, and Cecil Cheung. Central collaborations came via doctors and research coordinators. We thank Drs. Brian J. Czerniecki, Julia C. Tchou, Mark A. Rosen, Angela DeMichele, Mitchell D. Schnall, Gautham Mallampati, and Douglas L. Fraker. Also, we thank Monika Grosicka-Koptyra, Kathleen McCarthy, and Lauren Sherman for their significant contributions in recruiting patients. We thank Albert Cerussi, Bruce J. Tromberg, Hamid Dehghani, and Brian W. Pogue for providing figures for the chapter. For the illustrations, we thank Yookyung Choe. A.G.Y. acknowledges support from NIH grants R01-CA-75124, R01-HL-57835, and R01-EB-002109, from the U.S. Army under Cooperative Agreement DAMD17-00-1-0408, and from the NIH grant 1U54CA105480 from the National Cancer Institute, "Network for Translational Research in Optical Imaging (NTROI): Breast Cancer Multidimensional Diffuse Optical Imaging."

REFERENCES

1. D. B. Kopans, *Breast Imaging*, Lippincott-Raven, Philadelphia and New York, 1998.
2. American Cancer Society, *Statistics for 2004: Cancer Facts & Figures 2004*, http://www.cancer.org/docroot/STT/stt_0.asp (2004).
3. S. A. Feig, *Radiology* 167:659 (1988).
4. K. Kerlikowske, D. Grady, J. Barclay, E. A. Sickles, A. Eaton, and V. Ernster, *J. Am. Med. Assoc.* 276:39 (1996).
5. K. Kerlikowske, J. Barclay, D. Grady, E. A. Sickles, and V. Ernster, *J. Natl. Cancer Inst.* 89:76 (1997).
6. M. J. Homer, *Radiol. Clin. N. Am.* 23:459 (1985).
7. W. H. Hindle, L. Davis, and D. Wright, *Am. J. Obstet. Gynecol.* 180:1484 (1999).
8. C. J. Baines and R. Dayan, *J. Nail. Cancer Inst.* 91:833 (1999).
9. E. White, P. Velentgas, M. T. Mandelson, C. D. Lehman, J. G. Elmore, P. Porter, and Y. Yasui, and S. H. Taplin, *J. Natl. Cancer Inst.* 90:906 (1998).
10. Anonymous, *Mayo Clin. Health Lett. Suppl.* 1 (2001).
11. C. J. Bradley, C. W. Given, and C. Roberts, *Cancer* 91:178 (2001).
12. S. K. Goergen, J. Evans, G. P. Cohen, and J. H. MacMillan, *Radiology* 204:131 (1997).
13. R. L. Birdwell, D. M. Ikeda, K. F. O'Shaughnessy, and E. A. Sickles, *Radiology* 219:192(2001).
14. J. Wang, T. T. Shih, J. C. Hsu, and Y. W. Li, *Clin. Imaging* 24:96 (2000).
15. S. W. Fletcher, *J. Natl. Cancer Inst. Monogr.* 22:5 (1997).
16. J. Folkman, K. Watson, D. Ingber, and D. Hanahan, *Nature* 339:58 (1989).
17. P. Vaupel, O. Thews, D. K. Kelleher, and M. Hoeckel, *Adv. Exp. Med. Biol.* 454:591 (1998).
18. P. Vaupel, K. Schlenger, C. Knoop, and M. Hockel, *Cancer Res.* 51:3316 (1991).
19. N. Weidner, J. Folkman, F. Pozza, P. Bevilacqua, D. C. Allred, D. H. Moore, S. Meli, and G. Gasparini, *J. Natl. Cancer Inst.* 84:1875 (1992).
20. P. Vaupel and M. Hockel, *Int. J. Oncol.* 17:869 (2000).
21. J. R. Mourant, J. P. Freyer, A. H. Hielscher, A. A. Eick, D. Shen, and T. M. Johnson, *Appl. Opt.* 37:3586 (1998).
22. S. Thomsen and D. Tatman, *Ann. NY. Acad. Sci.* 838:171 (1998).
23. R. C. Haskell, L. O. Svaasand, T. Tsay, T. Feng, M. S. McAdams, and B. J. Tromberg, *J. Opt. Soc. Am. A* 11:2727 (1994).
24. M. A. Franceschini, K. T. Moesta, S. Fantini, G. Gaida, E. Gratton, H. Jess, W. W. Mantulin, M. Seeber, P. M. Schlag, and M. Kaschke, *Proc. Natl. Acad. Sci. U.S.A.* 94:6468 (1997).
25. S. B. Colak, M. B. van der Mark, G. W. Hooft, J. H. Hoogenraad, E. S. van da Linden, and F. A. Kuijpers, IEEE *J. Quantum Elect.* 5:1143 (1999).
26. V. Ntziachristos, A. G. Yodh, M. Schnall, and B. Chance, *Proc. Natl. Acad. Sci. USA* 97:2767 (2000).
27. B. J. Tromberg, N. Shah, R. Lanning, A. Cerussi, J. Espinoza, T. Pham, L. Svaasand, and J. Butler, *Neoplasia* 2:26 (2000).
28. B. W. Pogue, S. P. Poplack, T. O. McBride, W. A. Wells, K. S. Osterman, U. L. Osterberg, and K. D. Paulsen, *Radiology* 218:261 (2001).
29. H. Jiang, Y. Xu, N. Iftimia, J. Eggert, K. Klove, L. Baron, and L. Fajardo, *IEEE T. Med. Imaging.* 20:1334 (2001).

30. H. Dehghani, B. W. Pogue, S. D. Jiang, B. Brooksby, and K. D. Paulsen, *Appl. Opt.* 42:3117(2003).
31. A. Li, E. L. Miller, M. E. Kilmer, T. J. Brukilacchio, T. Chaves, J. Stott, Q. Zhang, T. Wu, M. Chorlton, R. H. Moore, D. B. Kopans, and D. A. Boas, *Appl. Opt.* 42:5181 (2003).
32. Q. I. Zhu, M. M. Huang, N. G. Chen, K. Zarfos, B. Jagjivan, M. Kane, P. Hedge, and S. H. Kurtzman, *Neoplasia* 5:379 (2003).
33. D. B. Jakubowski, A. E. Cerussi, F. Bevilacqua, N. Shah, D. Hsiang, J. Butler, and B. J. Tromberg, *J. Biomed. Opt.* 9:230 (2004).
34. R. Choe, A. Corlu, K. Lee, T. Durduran, S. D. Konecky, M. Grosicka-Koptyra, S. R. Arridge, B. J. Czerniecki, D. L. Fraker, A. DeMichele, B. Chance, M. A. Rosen, and A. G. Yodh, *Med. Phys.* 32:1128 (2005).
35. C. H. Schmitz, D. P. Klemer, R. Hardin, M. S. Katz, Y. Pei, H. L. Graber, M. B. Levin, R. D. Levina, N. A. Fraco, W. B. Solomon, and R. L. Barbour, *Appl. Opt.* 44:2140 (2005).
36. X. Intes, *Acad. Radiol.* 12:934 (2005).
37. D. Grosenick, K. T. Moesta, M. Möller, J. Mucke, H. Wabnitz, B. Gebauer, C. Stroszczynski, B. Wassermann, P. M. Schlag, and H. Rinneberg, *Phys. Med. Biol.* 50:2429 (2005).
38. D. Grosenick, H Wabnitz, K. T. Moesta, J. Mucke, P. M. Schlag, and H. Rinneberg, *Phys. Med. Biol.* 50:2451 (2005).
39. L. Spinelli, A. Torricelli, A. Pifferi, P. Taroni, G. Danesini, and R. Cubeddu, *Phys. Med. Biol.* 50:2489 (2005).
40. B. Chance, S. Nioka, J. Zhang, E. F. Conant, E. Hwang, S. Briest, S. G. Orel, M. D. Schnall, and B. J. Czerniecki, *Acad. Radiol.* 12:925 (2005).
41. A. Villringer and B. Chance, *Trends Neurosci.* 20:435 (1997).
42. G. Gratton, M. Fabiani, P. M. Corballis, D. C. Hood, M. R Goodman-Wood, J. Kirsch, K. Kim, D. Friedman, and E. Gratton, *Neuroimage* 6:168 (1997).
43. B. W. Pogue and K. D. Paulsen, *Opt. Lett.* 23:1716 (1998).
44. D. A. Benaron, S. R Hintz, A. Villringer, D. Boas, A. Kleinschmidt, J. Frahm, C. Hirth, H. Obrig, v. J. C, E. L. Kermit, W. Cheong, and D. K. Stevenson, *J. Cerebr. Blood F. Met.* 20:469477 (2000).
45. D. A. Boas, D. H. Brooks, E. L. Miller, C. A. DiMarzio, M. Kilmer, R. J. Gaudette, and Q. Zhang, *IEEE Signal Proc. Mag.* 18:57 (2001).
46. D. M. Hueber, M. A. Franceschini, H. Y. Ma, Q. Zhang, J. R. Ballesteros, S. Fantini, D. Wallace, V. Ntziachristos, and B. Chance, *Phys. Med. Biol.* 46:41 (2001).
47. A. Y. Bluestone, G. Abdoulaev, C. H. Schmitz, R. L. Barbour, and A. H. Hielscher, *Opt. Express* 9:272 (2001).
48. J. C. Hebden, A. Gibson, R. M. Yusof, N. Everdell, E. M. C. Hillman, D. T. Delpy, S. R. Arridge, T. Austin, J. H. Meek, and J. S. Wyatt, *Phys. Med. Biol.* 47:4155 (2002).
49. J. P. Culver, T. Durduran, T. Furuya, C. Cheung, J. H. Greenberg, and A. G. Yodh, *J. Cerebr. Blood F. Met.* 23:911 (2003).
50. J. Choi, M. Wolf, V. Toronov, U. Wolf, C. Polzonetti, D. Hueber, L. P. Safonova, R. Gupta, A. Michalos, W. Mantulin, and E. Gratton, *J. Biomed. Opt.* 9:221 (2004).
51. M. A. Franceschini and D. A. Boas, *Neurolmage* 21:372 (2004).
52. T. Durduran, Ph.D. dissertation, University of Pennsylvania (2004).
53. T. Wilcox, H. Bortfeld, R. Woods, E. Wruck, and D. A. Boas, *J. Biomed. Opt.* 10:011010(2005).
54. E. Gratton, V. Toronov, U. Wolf, M. Wolf, and A. Webb, *J. Biomed. Opt.* 10:11008 (2005).
55. J. R. Wilson, D. M. Mancini, K. McKully, J. Ferraro, V. Lanoce, and B. Chance, *Circulation* 80:1668 (1989).
56. B. Chance, M. T. Dait, C. Zhang, T. Hamaoka, and F. Hagerman, *Am. J. Physiol.* 262:C766 (1992).
57. R. A. De Blasi, M. Cope, C. Elwell, F. Safoue, and M. Ferrari, *Eur. J. Appl. Physiol. O.* 67:20 (1993).
58. T. Tamaki, S. Uchiyama, T. Tamura, and S. Nokana, *Eur. J. Appl. Physiol.* 68:465 (1994).
59. D. M. Mancini, L. Bolinger, H. Li, K. Kendrick, B. Chance, and J. R. Wilson, *J. Appl. Physiol.* 77:2740 (1994).
60. M. Jensen-Urstad, I. Hallback, and K. Sahlin, *Clin. Physiol.* 15:27 (1995).
61. S. Matsui, N. Tamura, T. Hirakawa, S. Kobayashi, N. Takekoshi, and E. Murakami, *Am. Heart J.* 129:690 (1995).
62. R. Belardinelli, T. J. Barstow, J. Porszasz, and K. Wasserman, *Med. Sci. Sport. Exer.* 27:487 (1995).
63. Y. Bhambhani, S. Buckley, and T. Susaki, *Med. Sci. Sport. Exer.* 29:402 (1997).
64. K. W. Rundell, S. Nioka, and B. Chance, *Med. Sci. Sport. Exer.* 29:248 (1997).
65. H. Otaga, T. Yunoki, and T. Yano, *Eur. J. Appl. Physiol.* 86:191 (2002).
66. U. Wolf, M. Wolf, J. H. Choi, L. A. Paunescu, L. P. Safonova, A. Michalos, and E. Gratton, *Adv. Exp. Med. Biol.* 510:225 (2003).
67. V. Quaresima, M. Ferrari, M. A. Franceschini, M. L. Hoimes, and S. Fantini, *J. Biomed. Opt.* 9:413 (2004).
68. B. C. Wilson, M. S. Patterson, and L. Lilge, *Laser. Med. Sci.* 12:182 (1997).
69. H. Wang, M. E. Putt, M. J. Emanuele, D. B. Shin, E. Glatstein, A. G. Yodh, and T. M. Busch, *Cancer Res.* 64:7553 (2004).
70. U. Sunar, H. Quon, T. Durduran, J. Zhang, J. Du, C. Zhou, G. Yu, R. Choe, A. Kilger, R. Lustig, L. Loevner, S. Nioka, B. Chance, and A. G. Yodh, *J. Biomed. Opt.*, 11:064021 (2006).

71. M. Cutler, *Surg. Gynecol. Obstet.* 48:721 (1929).
72. D. J. Watmough, *Radiology* 147:89 (1983).
73. E. A. Sickles, *Am. J. Roentgenol.* 142:841 (1984).
74. H. Wallberg, A. Alveryd, U. Bergvall, K. Nasiell, P. Sundelin, and S. Troel, *Act Radiol. Diagn.* 26:33 (1985).
75. A. E. Profio and G. A. Navarro. *Med. Phys.* 16:60 (1989).
76. A. Pera and A. K. Freimanis, *Obstet. Gynecol. Clin. N. Am.* 14:635 (1987).
77. E. N. Carlsen, *Diagn. Imaging* 4:28 (1982).
78. V. Marshall, D. C. Williams, and K. D. Smith, *Radiology* 150:339 (1984).
79. B. Monsees, J. M. Destouet, and W. G. Totty, *Radiology* 163:463 (1987).
80. J. J. Gisvold, L. R. Brown, R G. Swee, D. J. Raygor, N. Dickerson, and M. K. Ranfranz, *Am. J. Roentgenol.* 147:191 (1986).
81. R J. J. Bartrum and H. C. Crow, *Am. J. Roentgenol.* 142:409 (1984).
82. A. Yodh and B. Chance, *Phys. Today* 48:34 (1995).
83. B. Chance, Ed., in *Optical Tomography, Photon Migration, and Spectroscopy of Tissue and Model Media: Theory, Human Studies, and Instrumentation*, vol. 2389. SPIE, Bellingham, WA, 1995.
84. A. G. Yodh and D. A. Boas, in *Biomedical Photonics Handbook* (T. Vo-Dinh, Ed.), p. 21–1 to 21–45. CRC Press, Boca Raton, FL, 2003.
85. M. S. Patterson, B. Chance, and B. C. Wilson, *Appl. Opt.* 28:2331 (1989).
86. M. S. Patterson, J. D. Moulton, B. C. Wilson, K. W. Berndt, and J. R. Lakowicz, *Appl. Opt.* 30:4474 (1991).
87. E. Gratton, W. Mantulin, M. J. Ven, M. van de Ven, J. Fishkin, M. Maris, and B. Chance, in *Proceedings of The Third International Conference: Peace through Mind/Brain Science*, pp. 183–189. Hamamatsu, Japan. 1990.
88. D. T. Delpy, M. Cope, P. van der Zee, S. Arridge, S. Wray, and J. Wyatt. *Phys. Med. Biol.* 33:1433 (1988).
89. S. L. Jacques, *Appl. Opt.* 28:2223 (1989).
90. D. A. Benaron and D. K. Stevenson, *Science* 259:1463 (1993).
91. M. A. O'Leary, D. A. Boas, B. Chance, and A. G. Yodh, *Phys. Rev. Lett.* 69:2658 (1992).
92. J. B. Fishkin and E. Gratton, *J. Opt. Soc. Am. A* 10:127 (1993).
93. D. A. Boas, M. A. O'Leary, B. Chance, and A. G. Yodh. *Phys. Rev. E* 47:R2999 (1993).
94. J. M. Schmitt, A. Knuttel, and J. R. Knutson, *J. Opt. Soc. Am. A* 9:1832 (1992).
95. E. M. Sevick, J. R. Lakowicz, H. Szmacinski, K. Nowaczyk, and M. L. Johnson, *J. Photoch. Photobio. B* 16:169 (1992).
96. B. J. Tromberg, L. O. Svaasand, T. Tsay, and R. C. Haskell, *Appl. Opt.* 32:607 (1993).
97. B. C. Wilson, M. S. Patterson, and S. T. Flock, *Photoch. Photobio.* 46:601 (1987).
98. B. Chance, S. Nioka, J. Kent, K. McCully, M. Fountain, R. Greenfeld, and G. Holtom, *Anal. Biochem.* 174:698 (1988).
99. A. Hielscher, F. K. Tittel, and S. L. Jacques, in *Photon Migration and Imaging in Random Media and Tissues* (B. Chance, Ed.), vol. 1988, pp. 275–288. SPIE, Bellingham, WA, 1993.
100. M. Ferrari, D. A. Wilson, D. F. Hanley, J. F. Hartmann, M. C. Rogers, and R. J. Traystman, *Am. J. Physiol.* 256:H1493 (1989).
101. E. M. Sevick, B. Chance, J. Leigh, S. Nioka, and M. Maris, *Anal. Biochem.* 195:330 (1991).
102. M. Ferrari, Q. Wei, L. Carraresi, R. De Blasi, and G. Zaccanti, *J. Photoch. Photobio.* 16:141 (1992).
103. T. L. Duncan, L. Whitlock, M. Cope, and D. T. Delpy, in *Photon Migration and Imaging in Random Media and Tissues* (B. Chance, Ed.), vol. 1888. SPIE, Bellingham, WA, 1993.
104. L. O. Svaasand, B. J. Tromberg, R. C. Haskell, T. T. Tsay, and M. W. Berns, *Opt. Eng.* 32:258 (1993).
105. W. A. Wells, C. P. Daghlian, T. D. Tosteson, M. R. Grove, S. P. Poplack, S. Knowlton-Soho, and K. D. Paulsen, *Anal. Quant. Cytol. Histol.* 26:166 (2004).
106. Q. Zhu, S. H. Kurtzma, P. Hegde, S. Tannenbaum, M. Kane, M. Huang, N. G. Chen, B. Jagjivan, and K. Zarfbs, *Neoplasia* 7:263 (2005).
107. S. R. Arridge, *Inverse Probl.* 15:R41 (1999).
108. A. P. Gibson, J. C. Hebden, and S. R. Arridge, *Phys. Med. Biol.* 50:RI (2005).
109. M. C. Case and P. F. Zweifel, *Linear Transport Theory*, Addison-Wesley, New York, 1967.
110. B. Davison and J. B. Sykes, *Neutron Transport Theory*, Oxford University Press, London, 1957.
111. D. A. Boas, Ph.D. dissertation, University of Pennsylvania (1996).
112. T. Durduran, A. G. Yodh, B. Chance, and D. A. Boas, *J. Opt. Soc. Am. A* 14:3358 (1997).
113. M. Keijzer, W. M. Star, and P. Storch. *Appl. Opt.* 27:1820 (1988).
114. A. Lagendijk, R. Vreeker, and P. DeVries, *Phys. Lett. A* 136:81 (1989).
115. J. X. Zhu, D. J. Pine, and D. A. Weitz, *Phys. Rev. A* 44:3948 (1991).
116. R. A. J. Groenhuis, H. A. Ferwerda, and J. J. Ten Bosch, *Appl. Opt.* 22:2456 (1983).
117. B. W. Pogue and M. S. Patterson, *Phys. Med. Biol.* 39:1157 (1994).
118. B. W. Pogue and M. S. Patterson, *J. Biomed. Opt.* 1:311 (1996).
119. A. Kienle and T. Glanzmann, *Phys. Med. Biol.* 44:2689 (1999).
120. G. Alexandrakis, T. J. Farrell, and M. S. Patterson, *Appl. Opt.* 37:7401 (1998).

121. D. A. Boas, M. A. O'Leary, B. Chance, and A. G. Yodh, *P. Nail. Acad. Sci. USA* 91:4887(1994).
122. J. J. Duderstadt and L. J. Hamilton, *Nuclear Reactor Analysis*, Wiley, New York, 1976.
123. T. J. Farrel, M. S. Patterson, and B. Wilson, *Med. Phys.* 19:879 (1992).
124. R. Aronson, *J. Opt. Soc. Am. A* 12:2532 (1995).
125. A. C. Kak and M. Slaney, *Principles of Computerized Tomographic Imaging*, IEEE Press, New York, 1988.
126. M. A. O'Leary, Ph.D. dissertation, University of Pennsylvania (1996).
127. J. C. Schotland, J. C. Haselgrove, and J. S. Leigh, *Appl. Opt.* 32:448 (1993).
128. S. R. Arridge, *Appl. Opt.* 34:7395 (1995).
129. S. R. Arridge and M. Schweiger, *Appl. Opt.* 34:8026 (1995).
130. M. A. O'Leary, D. A. Boas, B. Chance, and A. G. Yodh, *Opt. Lett.* 20:426 (1995).
131. Y. Q. Yao, Y. Wang, Y. L. Pei, W. W. Zhu, and R. L. Barbour, *J. Opt. Soc. Am. A* 14:325 (1997).
132. K. D. Paulsen and H. Jiang, *Med. Phys.* 22:691 (1995).
133. S. R. Arridge and M. Schweiger, *Opt. Express* 2:213 (1998).
134. M. K. Simick, R. Jong, B. Wilson, and L. Lilge, *J. Biomed. Opt.* 9:794 (2004).
135. Z. Cheng, J. Mao, R. Bush, D. B. Kopans, R. H. Moore, and M. Chorlton, *Appl. Opt.* 42:6412 (2003).
136. C. H. Schmitz, M. Locker, J. M. Lasker, A. H. Hielscher, and R. L. Barbour, *Rev. Sci. Instrum.* 73:429 (2002).
137. N. Iftimia, X. J. Gu, Y. Xu, and H. B. Jiang, *Rev. Sci. Instrum.* 74:2836 (2003).
138. T. O. McBride, B. W. Pogue, S. Jiang, U. L. Osterberg, and K. D. Paulsen, *Rev. Sci. Instrum.* 72:1817 (2001).
139. N. G. Chen, P. Y. Guo, S. K. Yan, D. Q. Piao, and Q. Zhu, *Appl. Opt.* 40:6367 (2001).
140. S. Fantini, E. L. Heffer, M. A. Franceschini, L. Götz, A. Heinig, S. Heywang-Köbrunner, O. Schütz, and H. Siebold, in *Proceedings of Inter-Institute Workshop on In Vivo Optical Imaging at the NIH* (A. H. Gandjbakhche, Ed.), p. 111–117. Optical Society of America, Washington, DC, 2000.
141. Q. Zhang, T. J. Brukilacchio, A. Li, J. J. Stott, T. Chaves, E. Hillman, T. Wu, A. Chorlton, E. Raerty, R. H. Moore, D. B. Kopans, and D. A. Boas, *J. Biomed. Opt.* 10:024033 (2005).
142. A. Torricelli, L. Spinelli, A. Pifferi, P. Taroni, R. Cubeddu, and G. M. Danesini, *Opt. Express* 11:853 (2003).
143. D. Grosenick, K. T. Moesta, H. Wabnitz, J. Mucke, C. Stroszczynski, R. Macdonald, P. M. Schlag, and H. Rinneberg, *Appl. Opt.* 42:3170 (2003).
144. T. Dierkes, D. Grosenick, K. T. Moesta, M. Möller, P. M. Schlag, H. Rinneberg, and S. Arridge, *Phys. Med. Biol.* 50:2519 (2005).
145. F. E. W. Schmidt, M. E. Fry, E. M. C. Hillman, J. C. H den, and D. T. Delpy, *Rev. Sci. Instrum.* 71:256 (2000
146. F. Bevilacqua, A. J. Berger, A. E. Cerussi, Jakubowski, and B. J. Tromberg, *Appl. Opt.* 39:6- (2000).
147. J. P. Culver, R. Choe, M. J. Holboke, L. Zubkov, T. D duran, A. Slemp, V. Ntziachristos, B. Chance, and A. Yodh, *Med. Phys.* 30:235 (2003).
148. OMLC homepage, http://omlc.ogi.edu/spectra/ (cessed 2003).
149. J. R. Mourant, T. Fuselier, J. Boyer, T. M. Johnson, I. J. Bigio, *Appl. Opt.* 39:949 (1997).
150. A. M. K. Nilsson, C. Sturesson, D. L. Liu, and Andersson-Engels, *Appl. Opt.* 37:1256(1998).
151. T. Durduran, R. Choe, J. P. Culver, L. Zubkov, M. J. H boke, J. Giammarco, B. Chance, and A. G. Yodh, *Pl Med. Biol.* 47:2847 (2002).
152. A. Corlu, T. Durduran, R. Choe, M. Schweiger, E. C. Hillman, S. R. Arridge, and A. G. Yodh, *Opt. L* 28:2339 (2003).
153. A. Li, Q. Zhang, J. P. Culver, E. L. Miller, and D. Boas, *Opt. Lett.* 29:256 (2004).
154. A. Corlu, R. Choe, T. Durduran, K. Lee, M. Schweig S. R. Arridge, E. M. C. Hillman, and A. G. Yodh, *Ap Opt.* 44:2082 (2005).
155. S. Srinivasan, B. W. Pogue, S. Jiang, H. Dehghani, K. D. Paulsen, *Appl. Opt.* 44:1858(2005).
156. A. Li, G. Boverman, Y. Zhang, D. Brooks, E. L. Mil M. E. Kilmer, Q. Zhang, E. M. C. Hillman, and D. Boas, *Appl. Opt.* 44:1948 (2005).
157. G. Maret and P. E. Wolf, *Z. Phys.* 65:409 (1987).
158. D. J. Pine, D. A. Weitz, P. M. Chaikin, and E. H bolzheimer, *Phys. Rev. Lett.* 60:1134(1988).
159. D. A. Boas and A. G. Yodh, *J. Opt. Soc. Am. A* 14:1 (1997).
160. B. J. Ackerson, R. L. Dougherty, N. M. Reguigui, and Nobbman, *J. Thermophys. Heat Tr.* 6:577 (1992).
161. R. L. Dougherty, B. J. Ackerson, N. M. Reguigui, Dorri-Nowkoorani, and U. Nobbmann, *J. Quant. Sp trosc. Radiat. Transfer* 52:713 (1994).
162. D. A. Boas, L. E. Campbell, and A. G. Yodh, *Phys. R Lett.* 75:1855 (1995).
163. M. Heckmeier, S. E. Skipetrov, G. Maret, and R. M nard, *J. Opt. Soc. Am. A* 14:185 (1997).
164. S. O. Rice, in *Noise and Stochastic Processes* (N. W Ed.), p. 133. Dover, New York, 1954.
165. T. Durduran, R. Choe, G. Yu, C. Zhou, J. C. Tch B. J. Czerniecki, and A. G. Yodh, *Opt. Lett.* 30:29 (2005).
166. S. R. Arridge and W. R. B. Lionheart, *Opt. Lett.* 23:8 (1998).
167. Y. L Pei, H. L. Graber, and R. L. Barbour, *Opt. Expr* 9:97 (2001).
168. Y. Xu, X. Gu, T. Khan, and H. Jiang, *Appl. Opt.* 41:54 (2002).

169. Y. S. Yang, H. L. Liu, X. D. Li, and B. Chance, *Opt. Eng.* 36:1562 (1997).
170. D. Grosenick, H. Wabnitz, H. H. Rinneberg, K. T. Moesta, and P. M. Schlag, *Appl. Opt.* 38:2927 (1999).
171. B. Brooksby, S. D. Jiang, H Dehghani, B. W. Pogue, K. D. Paulsen, C. Kogel, M. Doyley, J. B. Weaver, and S. P. Poplack, *Rev. Sci. Instrum.* 75:5262 (2004).
172. A. Godavarty, M. J. Eppstein, C. Y. Zhang, S. Theru, A. B. Thompson, M. Gurnkel, and E. M. Sevick- Muraca, *Phys. Med. Biol.* 48:1701 (2003).
173. S. D. Jiang, B. W. Pogue, K. D. Paulsen, C. Kogel, and S. P. Poplack, *Opt. Lett.* 28:1212(2003).
174. S. Srinivasan, B. W. Pogue, S. D. Jiang, H. Dehghani, C. Kogel, S. Soho, J. J. Gibson, T. D. Tosteson, S. P. Poplack, and K. D. Paulsen, *P. Natl. Acad. Sci. USA* 100:12349(2003).
175. Y. Painchaud, A. Mailloux, E. Harvey, S. Verreault, J. Frechette, C. Gilbert, M. L. Vernon, and P. Beaudry, *Int. Symp. Biomed. Opt.* 3597:548 (1999).
176. B. Chance, *Ann. NY Acad. Sci.* 838:19(1998).
177. K. Suzuki, Y. Yamashita, K. Ohta, M Kaneko, M. Yoshida, and B. Chance, *J. Biomed. Opt.* 1:330(1996).
178. L. Spinelli, A. Torricelli, A. Pifferi, P. Taroni, G. M. Danesini, and R. Cubeddu, *J. Biomed. Opt.* 9:1137 (2004).
179. A. E. Cerussi, A. J. Berger, F. Bevilacqua, N. Shah, D. Jakubowski, J. Butler, R. F. Holcombe, and B. J. Tromberg, *Acad. Radiol.* 8:211 (2001).
180. X. Wang, B. W. Pogue, S. Jiang, X. Song, K. D. Paulsen, C. Kogel, S. P. Polack, and W. A. Wells, *J. Biomed. Opt.* 10:051704 (2005).
181. B. W. Pogue, S. D. Jiang, H. Dehghani, C. Kogel, S. Soho, S. Srinivasan, X. M. Song, T. D. Tosteson, S. P. Poplack, and K. D. Paulsen, *J. Biomed. Opt.* 9:541 (2004).
182. N. F. Boyd, G. A. Lockwood, J. W. Byng, D. L. Tritchler, and M. J. Yaffe, *Cancer Epidem. Biomar.* 7:1133 (1998).
183. K. Blyschak, M. Simick, R. Jong, and L. Lilge, *Med. Phys.* 31:1398 (2004).
184. N. Shah, A. Cerussi, C. Eker, J. Espinoza, J. Butler, J. Fishkin, R. Hornung, and B. Tromberg, *P. Natl. Acad. Sci. USA* 98:4420 (2001).
185. N. Shah, A. E. Cerussi, D. Jakubowski, D. Hsiang, J. Butler, and B. J. Tromberg, *J. Biomed. Opt.* 9:534 (2004).
186. T. Svensson, J. Swartling, P. Taroni, A. Torricelli, P. Lindblom, C. Ingvar, and S. Andersson-Engels, *Phys. Med. Biol.* 50:2559 (2005).
187. A. Cerussi, N. Shah, D. Hsiang, A. Durkin, J. Butler and B. J. Tromberg, *J. Biomed. Opt.* 11:044005 (2006).
188. V. E. Pera, E. L. Heer, H. Siebold, O. Schutz, S. Heywang-Kobrunner, L. Gotz, A. Heinig, and S. Fantini, *J. Biomed. Opt.* 8, 517 (2003).
189. E. Heffer, V. Pera, O. Schutz, H. Siebold, and S. Fantini, *J. Biomed. Opt.* 9:1152 (2004).
190. V. Chernomordik, D. W. Hattery, D. Grosenick, H. Wabnitz, H. Rinneberg, K. T. Moesta, P. M. Schlag, and A. Gandjbakhche, *J. Biomed. Opt.* 7:80 (2002).
191. D. Grosenick, H. Wabnitz, K. T. Moesta, J. Mucke, M. Moller, C. Stroszczynski, J. Stossel, B. Wassermann, P. M. Schlag, and H. Rinneberg, *Phys. Med. Biol.* 49:1165 (2004).
192. A. Pifferi, P. Taroni, A. Torricelli, F. Messina, R. Cubeddu, and G. Danesini, *Opt. Utt.* 28:1138(2003).
193. P. Taroni, G. Danesini, A. Torricelli, A. Pifferi, L. Spinelli, and R. Cubeddu, *J. Biomed. Opt.* 9:464 (2004).
194. P. Taroni, A. Torricelli, L. Spinelli, A. Pieri, F. Arpaia, G. Danesini, and R. Cubeddu, *Phys. Med. Biol.* 50:2469 (2005).
195. J. H. Hoogenraad, M. B. van der Mark, S. B. Colak, G. W. t'Hooft, and E. S. van der Linden, in *Photon Propagation of Tissues III* (D. A. Benaron, Ed), vol. 3194, p. 184–190. SPIE, Bellingham, WA, 1998.
196. H. B. Jiang, N. V. Iftimia, Y. Xu, J. A. Eggert, L. L. Fajardo, and K. L. Klove, *Acad. Radiol.* 9:186 (2002).
197. X. J. Gu, Q. Z. Zhang, M. Bartlett, L. Schutz, L. L. Fajardo, and H. B. Jiang, *Acad. Radiol.* 11:53 (2004).
198. T. Yates, J. C. Hebden, A. Gibson, N. Everdell, S. R. Arridge, and M. Douek, *Phys. Med. Biol.* 50:2503 (2005).
199. R. L. Barbour, H. L. Graber, C. H. Schmitz, F. Tarantini, G. Khoury, D. J. Naar, T. F. Panetta, T. Lewis, and Y. Pei, in *Optical Tomography and Spectroscopy of Tissue V*, (B. Chance, Ed.), vol. 4955, p. 84–92. SPIE, Bellingham, WA, 2003.
200. H. Dehghani, B. W. Pogue, S. P. Poplack, and K. D. Paulsen, *Appl. Opt.* 42:135 (2003).
201. S. Srinivasan, B. W. Pogue, H. Dehghani, S. D. Jiang, X. M. Song, and K. D. Paulsen, *J. Biomed. Opt.* 9:1161 (2004).
202. B. Brooksby, S. Srinivasan, S. Jiang, H Dehghani, B. W. Pogue, K. D. Paulsen, J. Weaver, C. Kogel, and S. P. Poplack, *Opt. Lett.* 30:1968 (2005).
203. D. Piao, S. Jiang, and B. W. Pogue, in *Optical Tomography and Spectroscopy of Tissue VI* (B. Chance, Ed.), vol. 5693. SPIE, Bellingham, WA, 2005.
204. H. Dehghani, B. W. Pogue, S. Jiang, S. Poplack, and K. D. Paulsen, in *Optical Tomography and Spectroscopy of Tissue* V (B. Chance, Ed.), vol. 4955. SPIE, Bellingham, WA, 2003.
205. R. Choe, Ph.D. dissertation, University of Pennsylvania (2005).
206. B. W. Pogue, S. P. Poplack, T. O. McBride, W. A. Wells, K. S. Osterman, and U. L. Osterberg, *Radiology* 214:609 (2000).
207. Q. Zhu, N. Chen, and S. H. Kurtzman, *Opt. Lett.* 28:337 (2003).
208. S. Fantini, S. A. Walker, M. A. Franceschini, M. Kaschke, P. M. Schlag, and K. T. Moesta, *Appl. Opt.* 37:1982 (1998).

209. T. O. McBride, B. W. Pogue, S. Poplack, S. Soho, W. A. Wells, S. D. Jiang, U. L. Osterberg, and K. D. Paulsen, *J. Biomed. Opt.* 7:72 (2002).

210. H. Madjar, W. Sauerbrei, H. J. Prömpeler, R. Wolfarth, and H. Guer, *Gynecol. Oncol.* 64:392 (1997).

211. J. P. Delille, P. J. Slanetz, E. D. Yeh, E. F. Halpern, D. B. Kopans, and L. Garrido, *Radiology* 228:63 (2003).

212. D. A. Mankoff, L. K. Dunnwald, J. R. Gralow, G. K. Ellis, E. K. Schubert, J. Tseng, T. J. Lawton, H. M. Linden, and R. B. Livinston, *J. Nucl. Med.* 44:1806 (2003).

213. R. E. Durand, *Cancer Metastasis Rev.* 20:57 (2001).

214. E. Bombardieri and F. Crippa, *Q. J. Nucl. Med.* 45:245 (2001).

215. R. P. Beaney, A. A. Lammertsma, T. Jones, C. G. McKenzie, and K. E. Halnan, *Lancet* 1:131 (1984).

216. C. B. Wilson, D. E. Snook, B. Dhokia, C. V. J. Taylor, I. A. Watson, A. A. Lammertsma, R. Lambrecht, J. Waxman, T. Jones, and A. A. Epenetos, *Int. J. Cancer* 47:344 (1991).

217. B. J. H. Wilson, A. A. Lammertsma, C. G. McKenzie, K. Sikora, and T. Jones, *Cancer Res.* 52:1592 (1992).

218. D. O. Cosgrove, J. C. Bamber, J. B. Davey, J. A. McKinna, and H. D. Sinnett, *Radiology* 176:175 (1990).

219. R. P. Kedar, D. O. Cosgrove, I. E. Smith, J. L. Mansi, and J. C. Bamber, *Radiology* 190:825 (1994).

220. D. Jakubowski, A. E. Cerussi, F. Bevilacqua, N. Shah, R Lanning, D. Hsiang, J. Butler, R. F. Holcombe, and B. J. Tromberg, *Laser. Surg. Med.* 1–1 (2002).

221. R. Tiling, R. Linke, M. Untch, A. Richter, S. Fieber, K. Brinkbaumer, K. Tatsch, and K. Hahn, *Eur. J. Nucl. Med.* 28:711 (2001).

222. A. Makris, T. J. Powles, S. Kakolyris, M. Dowsett, S. E. Ashley, and A. L. Harris, *Cancer* 85:1996 (1998).

223. G. Q. Yu, T. Durduran, C. Zhou, H. W. Wang, M. E. Putt, H. M. Saunders, C. M. Sehgal, E. Glatstein, A. G. Yodh, and T. M. Busch, *Clin. Cancer Res.* 11:3543 (2005).

224. J. C. Hebden, T. D. Yates, A. Gibson, N. Everdell, S. R. Arridge, D. W. Chicken, M. Douek, and M. R. S. Keshtgar, *Appl. Opt.* 44:1898 (2005).

225. R. W. Carlson and A. M. Favret, *Breast J.* 5, 303 (1999).

226. B. Fisher, J. Bryant, N. Wolmark, E. Mamounas, A. Brown, E. R. Fisher, D. L. Wickerham, M. Begovic, A. DeCillis, A. Robidoux, R. G. Margolese, A. B. J. Cruz, H. J. L, A. W. Lees, N. V. Dimitrov, and B. H. D, *J. Clin. Oncol.* 16:2672 (1998).

227. G. Cocconi, B. Di Blasio, G. Alberti, G. Bisagni, E Botti, and G Peracchia, *Breast Cancer Res. Tr.* 4:30 (1984).

228. M. C. Segel, D. D. Paulus, and G. N. Hortobagyi, *Radiology* 169:49 (1988).

229. S. J. Vinnicombe, A. D. MacVica, R. L. Guy, J. P. Sloan T. J. Powles, G. Knee, and J. E. Husband, *Radiolog.* 198:333 (1996).

230. L. Esserman, N. Hylton, L. Yassa, J. Barclay, S. Frankel and E. Sickles, *J. Clin. Oncol.* 17:110(1999).

231. P. J. Drew, M. J. Kerin, T. Mahapatra, C. Malone, J. R T. Monson, L. W. Turnbull, and J. N. Fox, *Eur. J. Surg Oncol.* 27:617 (2001).

232. M. V. Knopp, G. Brix, and S. L. Zeger, Magn. Reson *Imaging Clin. N. Am.* 2:633 (1994).

233. N. Tsuboi, Y. Ogawa, T. Inomata, D. Yoshida, S Yoshida, T. Moriki, and M. Kumon, *Oncol. Rep.* 6:72 (1999).

234. V. Ntziachristos, A. G. Yodh, M. D. Schnall, and B Chance, *Neoplasia* 4:347 (2002).

235. B. Brooksby, S. Jiang, H. Dehghani, B. W. Pogue, K D. Paulsen, J. Weaver, C. Kogel, and S. P. Poplack, *J Biomed. Opt.* 10:051504 (2005).

236. G. Boverman, E. L. Miller, A. Li, Q. Zhang, T. Chaves D. H. Brooks, and D. A. Boas, *Phys. Med. Biol.* 50:394 (2005).

237. N. Shah, J. Gibbs, D. Wolverton, A. Cerussi, N. Hylton and B. J. Tromberg, *J. Biomed. Opt.* 10:051503 (2005.)

238. Q. Zhu, T. Durduran, V. Ntziachristos, M. Holboke, an A. G. Yodh, *Opt. Lett.* 24:1050(1999).

239. M. J. Holboke, B. J. Tromberg, X. Li, N. Shah, J. Fishkin D. Kidney, J. Butler, B. Chance, and A. G. Yodh, *J Biomed. Opt.* 5:237 (2000).

240. Q. Zhu, E. Conant, and B. Chance, *J. Biomed. Opt.* 5:22 (2000).

241. X. Intes, J. Ripoll, Y. Chen, S. Nioka, A. G. Yodh, and B Chance, *Med. Phys.* 30:1039 (2003).

242. J. S. Reynolds, T. L. Troy, R. H. Mayer, A. B. Thomp son, D. J. Waters, K. K. Cornell, P. W. Snyder, and E. M Sevick-Muraca, *Photoch. Photobiol.* 70:87 (1999).

243. V. Ntziachristos and B. Chance, *Breast Cancer Res.* 3:4 (2001).

244. V. Ntziachristos, C. Bremer, E. E. Graves, J. Ripoll, an R. Weissleder, *Mol. Imaging* 1:82 (2002).

245. R. Weissleder and V. Ntziachristos, *Nat. Med.* 9:12 (2003).